Article

Cell Systems

Reserve Flux Capacity in the Pentose Phosphate Pathway Enables *Escherichia coli*'s Rapid Response to Oxidative Stress

Graphical Abstract

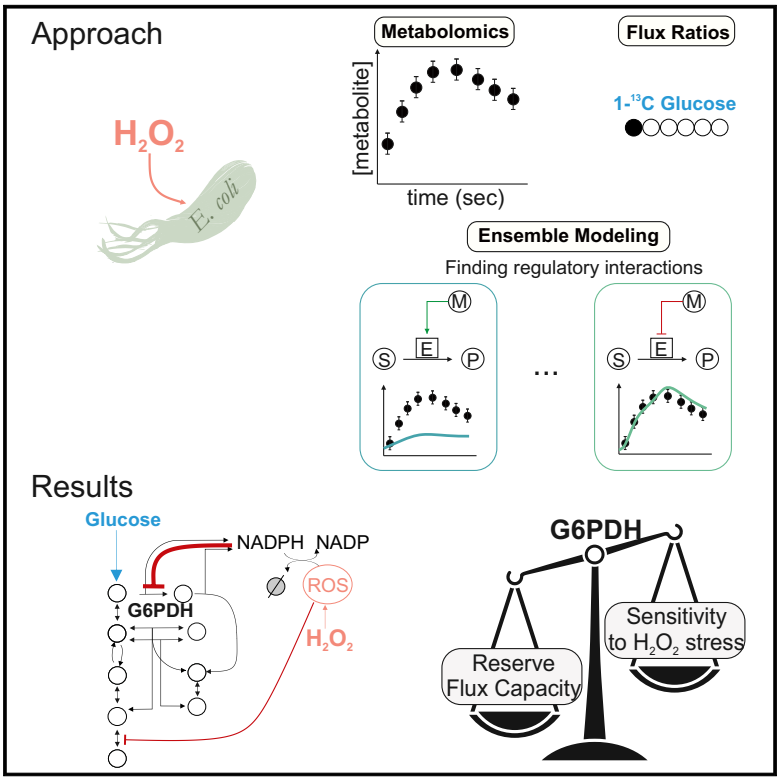

Highlights

- Characterization of the immediate metabolic response of *E. coli* to oxidative stress
- Development of a high-performance ensemble modeling computational pipeline
- Identification of NADPH feedback inhibition on G6PDH as key regulatory interaction
- Cells without reserve flux capacity in PP pathway are sensitive to oxidative stress

Authors

Dimitris Christodoulou, Hannes Link, Tobias Fuhrer, Karl Kochanowski, Luca Gerosa, Uwe Sauer

Correspondence

sauer@ethz.ch

In Brief

Christodoulou et al. describe the immediate metabolic response of *E. coli* to oxidative stress and reveal the key interactions that implement it. Combining quantitative metabolite dynamics with a high-performing ensemble modeling computational pipeline, they reveal the importance of a small molecule–protein interaction in the rapid cellular response. This interaction acts as a valve, maintaining a reserve of flux, which can be used rapidly when cells are exposed to stress. Cells without such a reserve capacity are more sensitive to oxidative stress.

Christodoulou et al., 2018, Cell Systems *6*, 569–578
May 23, 2018
https://doi.org/10.1016/j.cels.2018.04.009

CellPress

Cell Systems
Article

CellPress

Reserve Flux Capacity in the Pentose Phosphate Pathway Enables *Escherichia coli*'s Rapid Response to Oxidative Stress

Dimitris Christodoulou,[1,2] Hannes Link,[1,3] Tobias Fuhrer,[1] Karl Kochanowski,[1,4] Luca Gerosa,[1,5] and Uwe Sauer[1,6,*]
[1]Institute of Molecular Systems Biology, ETH Zurich, Zurich, Switzerland
[2]Systems Biology Graduate School, Zurich 8057, Switzerland
[3]Max Planck Institute for Terrestrial Microbiology, Marburg 35043, Germany
[4]Department of Pharmaceutical Chemistry, University of California, San Francisco, San Francisco, CA, USA
[5]Laboratory of Systems Pharmacology, Program in Therapeutic Science, Harvard Medical School, Boston, MA 02115, USA
[6]Lead Contact
*Correspondence: sauer@ethz.ch
https://doi.org/10.1016/j.cels.2018.04.009

SUMMARY

To counteract oxidative stress and reactive oxygen species (ROS), bacteria evolved various mechanisms, primarily reducing ROS through antioxidant systems that utilize cofactor NADPH. Cells must stabilize NADPH levels by increasing flux through replenishing metabolic pathways like pentose phosphate (PP) pathway. Here, we investigate the mechanism enabling the rapid increase in NADPH supply by exposing *Escherichia coli* to hydrogen peroxide and quantifying the immediate metabolite dynamics. To systematically infer active regulatory interactions governing this response, we evaluated ensembles of kinetic models of glycolysis and PP pathway, each with different regulation mechanisms. Besides the known inactivation of glyceraldehyde 3-phosphate dehydrogenase by ROS, we reveal the important allosteric inhibition of the first PP pathway enzyme by NADPH. This NADPH feedback inhibition maintains a below maximum-capacity PP pathway flux under non-stress conditions. Relieving this inhibition instantly increases PP pathway flux upon oxidative stress. We demonstrate that reducing cells' capacity to rapidly reroute their flux through the PP pathway increases their oxidative stress sensitivity.

INTRODUCTION

Bacteria continuously face environmental challenges that range from nutrient fluctuations to physicochemical stresses. A frequent challenge is oxidative stress because respiratory metabolism produces reactive oxygen species (ROS) that chemically damage cellular components (Mishra and Imlay, 2012; Imlay, 2013). Several evolved metabolic and other responses counter the detrimental effects by detoxifying ROS and alleviating acute damages on short and longer time scales (Greenberg and Demple, 1989; Brumaghim et al., 2003; Blanchard et al., 2007; Grant, 2008; Ralser et al., 2009; Rui et al., 2010; Krüger et al., 2011; Mishra and Imlay, 2012; Baez and Shiloach, 2013; Shimizu, 2013).

In the facultative aerobe *Escherichia coli*, the long-term defense against ROS is coordinated by the transcription factors OxyR and the SoxRS (Zheng and Storz, 2000; Seo et al., 2015), the former of which responds primarily to the ROS hydrogen peroxide (H_2O_2) (Nunoshiba et al., 1992). Since gene expression-based responses require minutes to become effective (Chechik et al., 2008), immediate responses must rely on already present anti-oxidative systems such as superoxide dismutase, catalases, glutathione peroxidase, and non-enzymatic antioxidants like the reducing agent glutathione to scavenge ROS (Kohen and Nyska, 2002; Finkel, 2003). In steady state, the pool of reduced glutathione is continuously replenished through redox reactions in central metabolism. Upon sudden oxidative stress, however, the cellular redox state must be stabilized immediately to circumvent stalling of anabolic reactions and thus potential death. From bacteria to humans cells, most organisms increase the reduction rate of $NADP^+$ to NADPH mainly by rerouting their glycolytic flux into the pentose phosphate (PP) pathway (Ralser et al., 2007; Rui et al., 2010; Anastasiou et al., 2011; Kuehne et al., 2015). The prevailing model stipulates that ROS directly oxidize lower glycolytic enzymes (Ralser et al., 2009) and thereby block glycolytic flux, such that upstream accumulating intermediates passively cause the rapid rerouting into the PP pathway (Ralser et al., 2007, 2009). This oxidative block of glycolysis was an important discovery, but it is presently not clear whether it is sufficient to achieve the rapid flux rerouting. Indeed, inconsistent with this model, hexose levels in mammalian cells do not increase prior to accumulation of PP pathway intermediates (Kuehne et al., 2015).

To understand the combination of flux regulating mechanisms necessary to achieve the immediate replenishment of NADPH for glutathione reduction upon sudden oxidative stress in *E. coli*, we determined the dynamic metabolome and ^{13}C-tracer response within the first minute after exposure to H_2O_2. For data interpretation, we developed a computational framework that evaluates ensembles of thousands of kinetic models of glycolysis and the PP pathway, each with different combinations of regulation mechanisms. Our computational framework was implemented

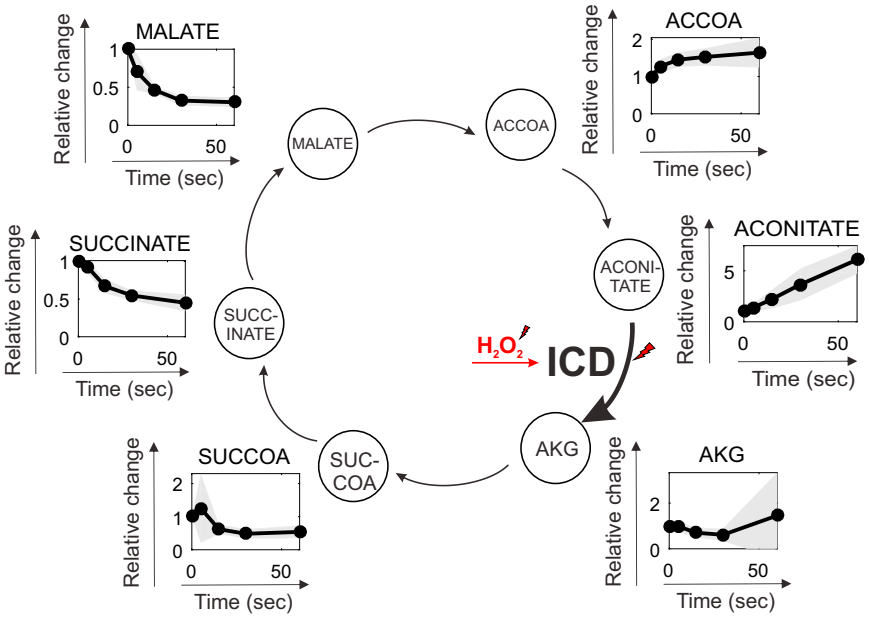

Figure 1. Profiles of the TCA Cycle Intermediates upon H_2O_2 Treatment

The changes of each metabolite relative to the untreated condition (time point 0) are shown, see also Table S6. Solid black lines represent the average relative change from three independent biological experiments, with the shaded area denoting the SD.

using concepts from parallel computing, allowing the efficient evaluation of large numbers of structurally distinct kinetic models. This enables unbiased identification of novel regulatory interactions and quantitative assessment of their function in a network context. By rigorous testing of these models against the experimental data, we identify the most relevant molecular interactions required for the rapid flux rerouting from glycolysis to the PP pathway and validate them *in vitro*. Our results challenge the current model for this flux rerouting and reveal a large reserve capacity in the PP pathway under normal steady-state growth conditions.

RESULTS

The Immediate Metabolic Response of *E. coli* to H_2O_2 Stress

To identify the timescale of the immediate oxidative stress response, we challenged *E. coli* cultures growing exponentially on glucose with 1 mM H_2O_2 using a variant of the filter cultivation method (Yuan et al., 2008; Link et al., 2013), and followed the dynamics of 30 intracellular metabolites for up to 1 min. The continuous increase of aconitate, up to 6-fold, together with the decrease of succinate, succinyl-CoA, and malate in the tricarboxylic acid (TCA) cycle (Figure 1), are consistent with the known strong reduction of isocitrate dehydrogenase activity upon exposure to oxidative stress (Murakami et al., 2006; Sandoval et al., 2011). Declining levels of the redox cofactor NADPH indicate its consumption for the ROS defense (Figure 2A). The most rapid responses, already within 5 s, occurred in all measured PP pathway intermediates, most pronounced for 6-phosphogluconate in the oxidative branch (Figure 2A). Responses in glycolysis were much slower with a gradual increase and decrease over 30 s for fructose-1,6 bisphosphate (FBP) and phosphoenolpyruvate, respectively. Hexose phosphate levels in upper glycolysis remained invariant. Increasing PP pathway intermediate and FBP levels and decreasing phosphoenolpyruvate levels upon oxidative stress are consistent with observations from yeast and mammalian cells (Ralser et al., 2009; Kuehne et al., 2015).

To elucidate oxidative stress-triggered flux changes that cause the rapid metabolite dynamics, we repeated the experiment by perfusing cells on filter with H_2O_2 and a medium containing [1-^{13}C] glucose. From liquid chromatography-tandem mass spectrometry-determined dynamic isotope distributions (Link et al., 2013), we quantified the ratio of unlabeled versus labeled fructose-6-phosphate to estimate relative flux changes through the PP pathway. Since the carbon at position 1 of glucose is liberated as CO_2 in the oxidative PP pathway, increasing proportions of PP pathway flux relative to glycolysis will lower the fractional labeling of fructose-6-phosphate (Figure 2B). Our results provide a lower bound for the oxidative PP pathway flux and show that at least 13% of glucose catabolism proceeds through the PP pathway during unstressed growth, which doubles to at least 28% about 1 min after oxidative stress (Figure 2C). A similarly rapid and strong flux increase in the PP pathway flux for regeneration of NADPH to fuel the glutathione system has been reported in other organisms (Kuehne et al., 2015). This flux rerouting occurs well before *E. coli* can change enzyme abundance, and hence suggests either substrate or allosteric regulation. Since hexose phosphate levels remain constant during this time frame, the previously postulated block in glycolytic flux and substrate-mediated overflow into the PP pathway (Ralser et al., 2007) cannot be the only explanation. Instead, our results strongly suggest that *E. coli* does not use the full flux capacity of the oxidative PP pathway enzymes during growth on glucose such that the flux can be increased without enzyme synthesis. This result is consistent with the discrepancy between *in vitro*-determined maximal enzyme activities in the oxidative PP pathway of approximately 3.2 mmol g^{-1} h^{-1} (Fuhrer and Sauer, 2009) and the about 40% lower actual intracellular fluxes of 2.0 mmol g^{-1} h^{-1} reported previously (Fuhrer et al., 2005; Park et al., 2016).

Model-Based Identification of Mechanisms that Enable Rapid Adaptation to Oxidative Stress

How does *E. coli* rapidly mobilize this "reserve flux capacity" in the PP pathway? To identify the mechanism, we developed a mathematical model of glycolysis and PP pathway with 12 ordinary differential equations that consists of 12 metabolites (state variables) and 26 reactions, able to represent

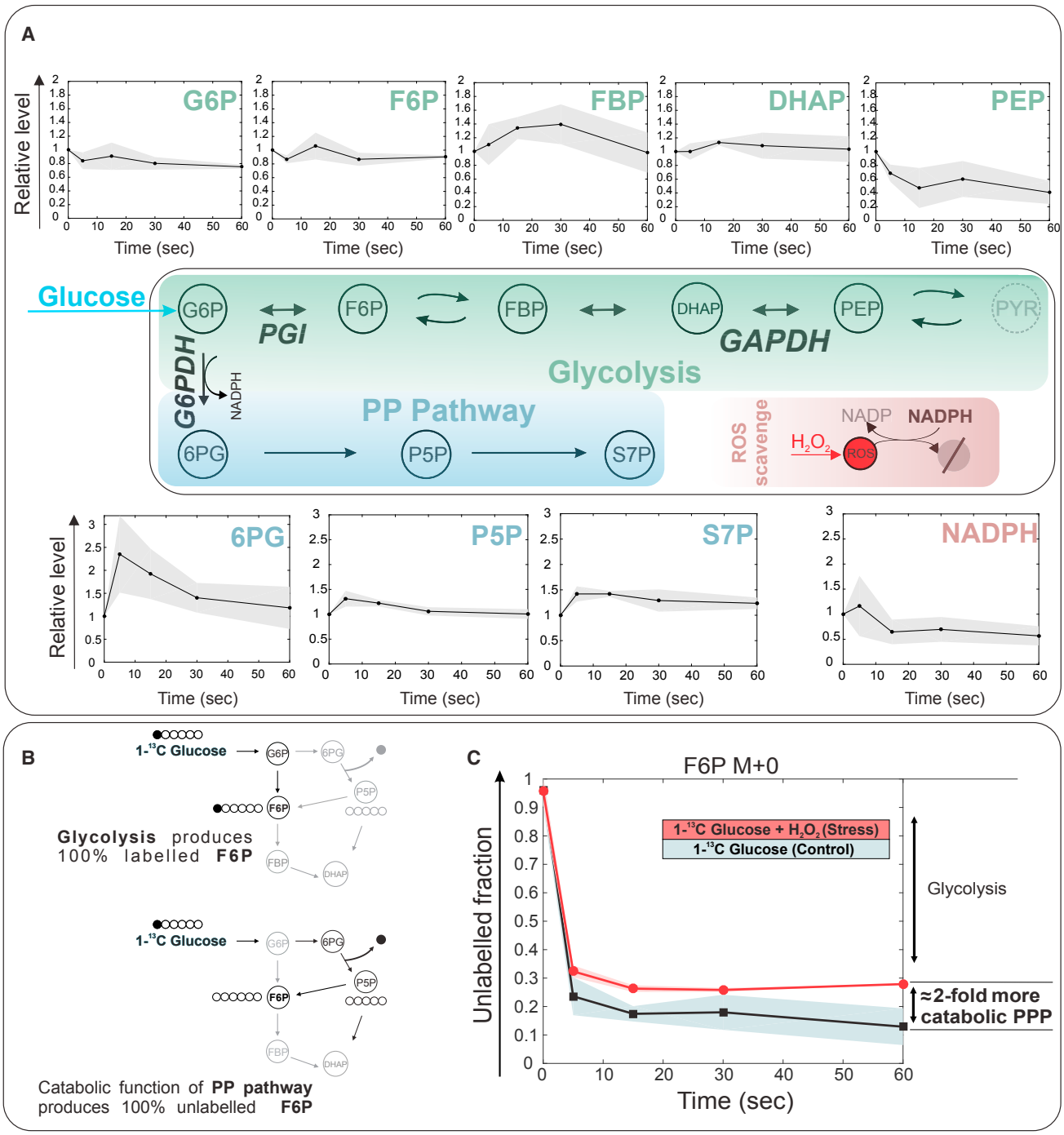

Figure 2. The Immediate Metabolic Response of *E. coli* to Oxidative Stress

(A) Profiles of glycolytic and PP pathway intermediates, upon H_2O_2 treatment of glucose-grown cells on filter (see STAR Methods). The changes of each metabolite relative to the untreated condition (time point 0) are shown, see also Table S6. Solid black lines represent the average relative change from three independent biological experiments, with the shaded area denoting the SD. Abbreviations are as follows: G6P, glucose 6-phosphate; F6P, fructose 6-phosphate; DHAP, dihydroxyacetone phosphate; 6PG, 6-phospho gluconate; P5P, pentose 5-phosphate.

(B) When cells are treated with medium containing [1-^{13}C]glucose, the 1-C of glucose is liberated as CO_2 in the oxidative PP pathway. By measuring the unlabeled versus the labeled fraction of F6P we can quantify the ratio of the flux that goes through glycolysis (producing 100% labeled F6P) and the flux that goes through the catabolic PP pathway (producing 100% unlabeled F6P).

(C) Relative changes in flux through the PP pathway. The experiment was performed by perfusing cells on the filter with a medium containing [1-^{13}C] (M+1) glucose with or without H_2O_2. Time point 0 represents the culture prior to label perfusion and subsequently filters were removed and cells immediately quenched

(legend continued on next page)

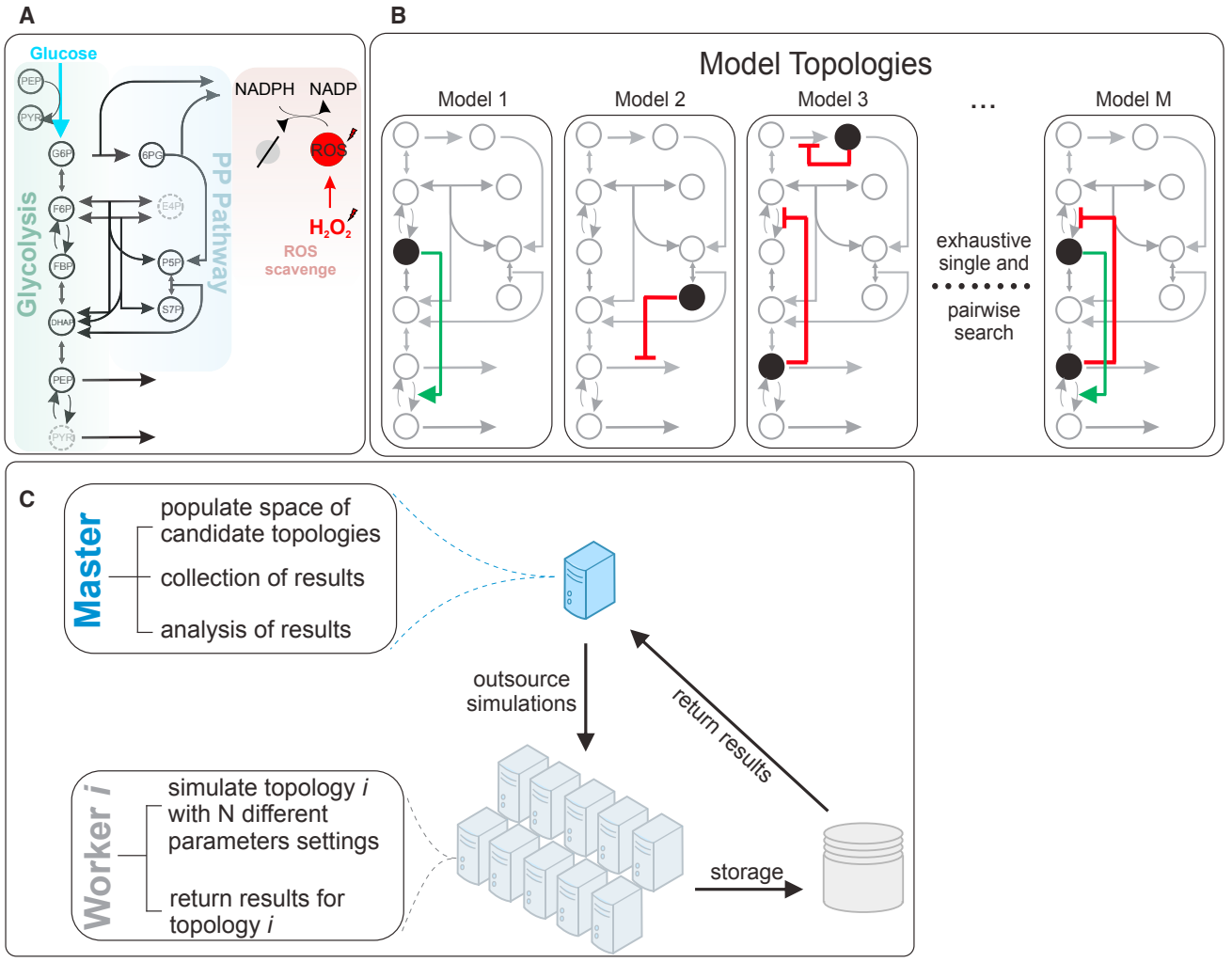

Figure 3. Inference of *In Vivo* Functional Metabolite-Enzyme Interactions and the Parallel Computational Framework that Implements It

(A) Representation of the system we consider for the implemented computational models, for growth on glucose. Black arrows indicate biochemical reactions, with reversible reactions indicated by arrows in both directions (see also Table S2). ROS is a state variable in our system, and is scavenged by consumption of NADPH. Every irreversible reaction can be a target for activation of inhibition of each one of the state variables of our system.

(B) Metabolite-enzyme interactions are exhaustively tested in single interactions and in pairs. Each of the approximately 12,000 model topologies is simulated at least 2,000 times with different parameters to account for parametric uncertainty in the kinetics. Each model of the approximately 24 million models is simulated and then evaluated based on its capacity to describe the dynamic experimental metabolite data.

(C) Parallel computational framework for the evaluation of millions of kinetic models on their capacity to explain the experimental data. The framework allows the simulation of millions of kinetic models by the distributed, parallel execution of many simulations by different workers-CPU processors (see also STAR Methods).

glutathione detoxification of ROS by the oxidation of NADPH (Figure 3A). Kinetics of reversible and irreversible reactions were modeled with mass action and Michaelis-Menten laws, respectively. The binding constants (K_M) were randomly sampled in a 0.1–10 times range around their literature values to account for potential parametric uncertainty. Maximum reaction rates (V_{max}) were calculated from flux distributions during steady-state growth on glucose, as was described before (Link et al., 2013) (Supplemental Information) and the ROS flux was treated as a free parameter. If inhibition of glyceraldehyde 3-phosphate (GAP) dehydrogenase was sufficient to explain metabolite dynamics and flux rerouting (Ralser et al., 2007, 2009), amending the above model with direct ROS inhibition of lower glycolysis should capture the experimentally determined metabolite dynamics. While this amended base model was indeed able to describe glycolysis dynamics to some extent, it failed entirely to describe the PP pathway dynamics (Figure S1), suggesting that, akin to

at the indicated time points after label perfusion. Changes in the fraction of unlabeled fructose-6-phosphate of cells perfused with [1-^{13}C] glucose on filter in the two different cases are shown. The control experiment (no H_2O_2 stress), is represented with a black line which shows the average of two individual biological replicates, with the gray-shaded area representing the SD. Treatment with H_2O_2 stress is represented with a red line which shows the average of two individual biological replicates, with the red shaded area representing the SD.

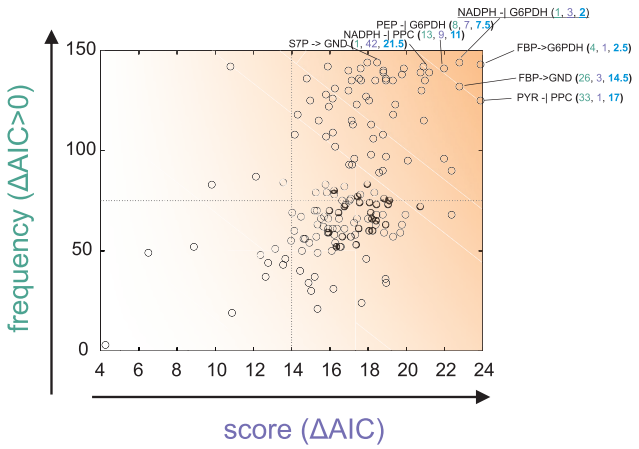

Figure 4. Relevance of Allosteric Interactions Based on the Frequency of Occurrence in Models that Improve the Base Model and the Information Content of the Best Model with This Interaction (ΔAIC)

For the selected interactions, in parenthesis, the different ranks this interaction achieved in frequency, score and in the overall averaged rank, are shown. The type of interaction is indicated as activation (->) and inhibition (-l).

Table 1. Rank of the Best Ten Interactions, as Inferred from the Combined Computational-Experimental Approach

#	Enzyme	Metabolite	Activation/ Inhibition	Pairwise Average Rank
1	G6PDH	NADPH	(–)	2.0
2	G6PDH	FBP	(+)	2.5
3	G6PDH	PEP	(–)	7.5
4	PFK	S7P	(+)	8.5
5	PPC	NADPH	(–)	11.0
6	PPS	NADPH	(+)	13.0
7	PYK	S7P	(–)	13.5
8	GND	FBP	(+)	14.5
9	PYK	NADPH	(–)	15.0
10	PPC	PYR	(–)	17.0

Pairwise average rank (fifth column, Table 1) was calculated as the average of the different ranks each interaction achieved in individual metrics, namely frequency and score, stemming from the results of approximately 24 million pairwise simulations. Enzymes affected by metabolites (activated or inhibited) are shown in columns 2, 3, and 4 of the table, respectively (see also Tables S3 and S4). Abbreviations: G6PDH, glucose 6-phosphate dehydrogenase; GND, phosphogluconate dehydrogenase; PFK, phosphofructokinase; PPC, phosphoenolpyruvate carboxylase; PPS, phosphoenolpyruvate synthase; NADPH, nicotinamide adenine dinucleotide phosphate; FBP, fructose bisphosphate; PEP, phosphoenolpyruvate; S7P, sedoheptulose 7-phosphate; PYR, pyruvate.

mammalian cells (Kuehne et al., 2015), inhibition of GAP dehydrogenase is perhaps necessary but not sufficient.

To identify putative missing allosteric regulation, we systematically tested activation and inactivation of each irreversible reaction by metabolites through adding a power law term that affects the maximum reaction rate. Reversible reactions were not tested systematically to reduce the computational complexity of the topological search and because there is scarce evidence for their regulation by small molecules (Reznik et al., 2017). To further reduce the complexity, metabolites with similar signals, such as the hexose phosphates, were lumped (Link et al., 2013) and metabolites such as dihydroxyacetone phosphate (DHAP) that do not change over time were excluded from the analysis (Figure 2). We thereby generated an ensemble of about 12,000 structurally different models, by first compiling all single activating and inhibiting interactions of nine irreversible enzymes times nine metabolites, and consequently combining all pairs from this set, excluding the cases where two metabolites act on the same enzyme. Each structurally different model consists of the base model with GAP dehydrogenase inhibition by ROS plus two additional putative allosteric interactions (Figure 3B). As above, the kinetic parameters K_M and V_{max} were randomly sampled 2,000 times around their literature values for each model, thus requiring 24 million simulations in total (see also Table S2). Such a large number of simulations typically precludes systematic evaluation of structural and parametric uncertainties in kinetic models (Jia et al., 2012; Sunnaker et al., 2013, 2014; Babtie et al., 2014; Link et al., 2014). To overcome this limitation at a reasonable computation time, we used concepts from parallel computing and developed a scalable framework to perform thousands of simulations in parallel (Figure 3C, Supplemental Information). Using our parallel framework, we tested all 12,000 models for their capacity to describe the metabolite dynamics after exposure to H_2O_2 stress. The information content of these models was assessed by the Akaike information criterion that quantifies the capacity to describe the data and penalizes for additional interactions/parameters (Turkheimer et al., 2003). This analysis provides us with two quantitative measures that can be used to evaluate the biological relevance of a given interaction; i.e., the frequency at which individual interactions occur in models that improved the amended base model and the score of information content achieved by the best model carrying these interactions (Figure 4).

The results of these computations show that glucose-6-phosphate (G6P) dehydrogenase and phosphogluconate dehydrogenase in the oxidative branch of the PP pathway occur at high frequency as putative allosteric regulation targets in the good models and also achieve the highest scores (Figure 4 and Table S4). In particular, increase of the G6P dehydrogenase activity was key to improve the base model, and the most prominent interaction that mechanistically achieved this activation was relief from NADPH inhibition, which is rapidly reduced upon stress (Figure 2A). In fact, this NADPH inhibition of G6P dehydrogenase improved the base model in combination with any of the 144 possible regulation pairs (Table S4). Our modeling framework is primarily a hypothesis-generation tool in which different putative interactions (or combinations thereof) may achieve similar model responses. To identify those that most probably occur *in vivo*, we evaluated the different interactions in the 24 million simulations (i.e., 2,000 runs for each of the 12,000 models) by calculating the overall rank for every interaction, based on the average of the different ranks each interaction achieved in frequency and score (Tables 1 and S3). The by far highest rank was achieved by NADPH inhibition and FBP activation of G6P dehydrogenase, followed with quite a distance by phosphoenolpyruvate (PEP) inhibition of G6P dehydrogenase.

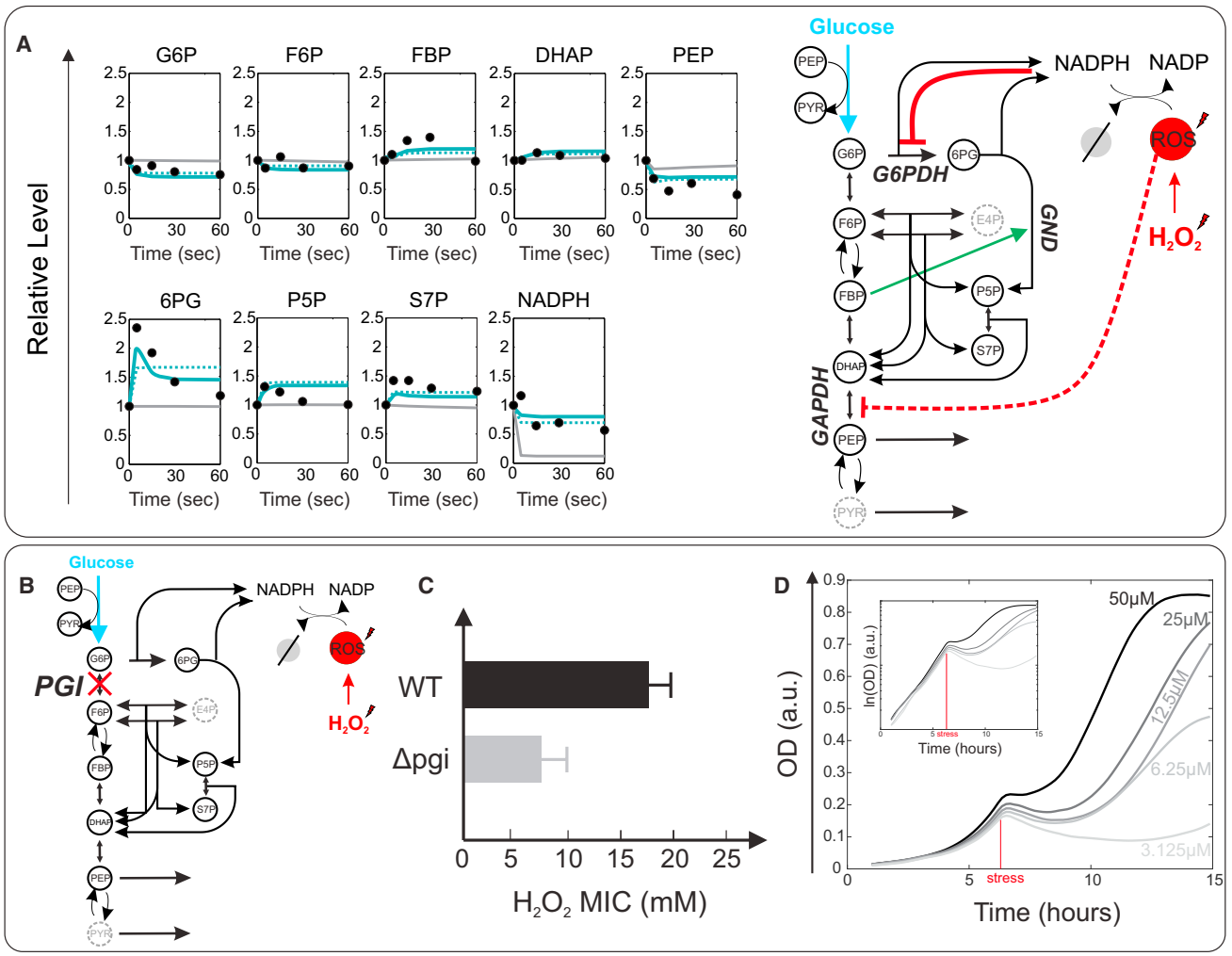

Figure 5. Results from the Model-Based Identification of Mechanisms that Enable Rapid Adaptation and the Importance of the Reserve Capacity of Flux in G6P Dehydrogenase

(A) *In silico* relevance of ROS oxidation (inhibition) of lower glycolysis and NADPH inhibition of G6P dehydrogenase. Black dots represent the dynamic experimental data, the gray line shows simulation results of the amended base model (with ROS inhibitory interaction to lower glycolysis, see also Figure S1). Blue dashed lines show the simulation results of the best single interaction model, NADPH inhibition of G6P dehydrogenase. Blue solid lines show the simulation results of the best pairwise interaction model, which includes NADPH inhibition of G6P dehydrogenase and activation of phosphogluconate dehydrogenase by FBP (see also Tables S3, S4, and S5).

(B) G6P isomerase deletion mutants (Δ*pgi*) are blocked in upper glycolysis and rely exclusively on the PP pathway for glucose catabolism.

(C) Importance of reserve flux capacity for cell tolerance against oxidative stress. Δ*pgi* mutants are less tolerant to H_2O_2 mediated oxidative stress, with approximately half the H_2O_2 minimal inhibitory concentration (MIC) wild-type (WT) strains have.

(D) Growth of a titratable G6P dehydrogenase *E. coli* strain before and after challenge with 20 mM of H_2O_2. The black line corresponds to approximately WT expression level (see also Figure 6G) and decreasing shades of gray represent lower expression levels, as indicated by the isopropyl β-D-1-thiogalactopyranoside (IPTG) induction levels above each line. The H_2O_2 dosage was chosen as the MIC of the WT (Figure 5C). Inset: the same data are shown in log scale. Growth rates before the oxidative stress treatment are reported in Figure 6.

To differentiate between the two most probable mechanisms of modulating G6P dehydrogenase activity, we determined the enzyme's kinetic parameters *in vitro* (see Table S1). While FBP does not alter G6P dehydrogenase activity at the tested concentration of 2 mM (see Table S1), we observed strong inhibition by NADPH with a K_I in the range of 15–35 μM (Table S1), as has been previously reported but without offering a quantitative functional understanding in the network context (Sanwal, 1970; Olavarría et al., 2012). This strong inhibition by NADPH seems to be the reason for the previously discussed discrepancy of approximately 40% between maximal *in vitro* activity and *in vivo* G6P dehydrogenase fluxes, since simulated initial reaction velocities of the enzyme decrease significantly when NADPH inhibition is included (Figure S2).

The remaining question is how relevant this NADPH inhibition is *in vivo*; i.e., how well it can explain the data already on its own. For this purpose, we tested all 162 models with only single putative regulatory interactions in addition to the known ROS inactivation of GAP dehydrogenase by extensive random sampling of the parameter space 20,000 times. Consistent with

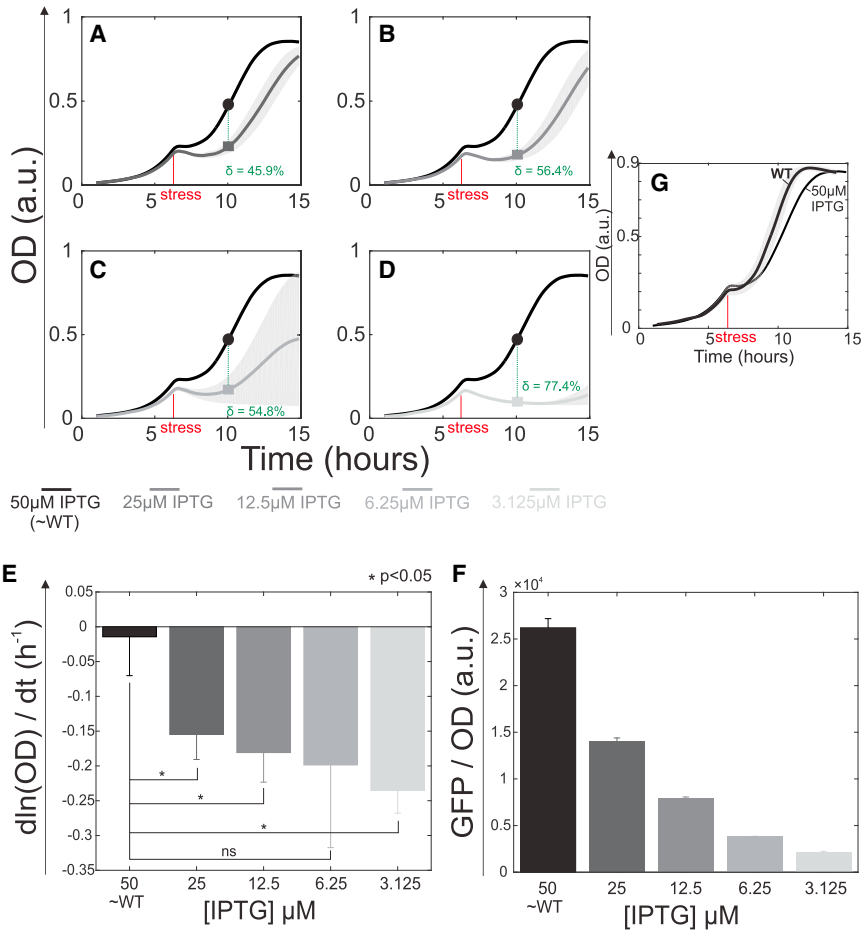

Figure 6. The Titratable G6P Dehydrogenase *E. coli* Strain with Reduced Levels of G6P Dehydrogenase—and Therefore Reduced Level of Reserve Capacity—Is Impaired When Exposed to Oxidative Stress

(A–D) The titratable G6P dehydrogenase *E. coli* strain with approximately the wild-type (WT) levels of the enzyme (black line) was challenged with 20 mM of H_2O_2 stress, which was found to be the MIC of H_2O_2 for WT *E. coli* (Figure 5C). The optical density (OD) of the culture was measured over time and growth rates were calculated before and after oxidative stress treatment. The same experiment and calculations were performed for different titration levels that translate to lower enzyme levels. These are shown with different gray shades: the lighter the shade the lower the enzyme level. Solid lines represent the average OD value at each time point and the shaded area denotes the SD. To quantify the effect the different enzyme levels (and reserve capacity levels) have on the fitness of the culture, we calculated the value

$$\delta = \frac{\frac{OD_{WT_{post\_stress}}}{OD_{WT_{pre\_stress}}} - \frac{OD_{X_{post\_stress}}}{OD_{X_{pre\_stress}}}}{\frac{OD_{WT_{post\_stress}}}{OD_{WT_{pre\_stress}}}},$$

where $OD_{WT_{post\_stress}}$ is the OD value of the strain induced with 50 μM of IPTG approximately 4 hours after the insult of 20 mM of H_2O_2. $OD_{WT_{pre\_stress}}$ is the OD value of the same strain, just before the stress was applied to the growing cells. Similarly, $OD_{X_{post\_stress}}$ is the OD value of any of the other four cases (induction with 25, 12.5, 6.25, or 3.125 μM of IPTG) after stress and $OD_{X_{pre\_stress}}$ just before stress. This value δ provides an estimate of how much loss of fitness the strains experience, relative to the highest induced strain (approximating WT).

(E) The mean of the minimum values of the dln(OD)/dt is shown, for each strain, indicating the maximum effect the stress can have in the culture in terms of rate of change of the ln(OD). Stars denote statistically significant differences, ns denotes non-significant differences. In particular: p value (50 versus 25) = 0.03, p value (50 versus 12.5) = 0.02, p value (50 versus 6.25) = 0.07, p value (50 versus 3.125) = 0.02 (t test function, MATLAB).

(F) Mean expression level of G6P dehydrogenase in the five different titration levels, normalized for the OD of every culture. Error bars denote the SD from two biological replicates.

(G) WT *E. coli* OD measurements over time, treated with 20 mM H_2O_2 stress at the indicated time against the titratable G6P dehydrogenase *E. coli* strain treated with 50 μM IPTG and stressed at the (same) indicated time. Black lines show mean values and shaded gray areas show SD as defined by at least two biological replicates. Pre-stress average growth rates of the titratable G6P dehydrogenase strain with different IPTG level: 50 μM – 0.56 hr^{-1}, 25 μM – 0.56 hr^{-1}, 12.5 μM – 0.57 hr^{-1}, 6.25 μM – 0.57 hr^{-1}, 3.125 μM – 0.55 hr^{-1}.

our previous results, NADPH inhibition of G6P dehydrogenase was again the best model topology (Table S5). This single interaction model could already explain the PP pathway metabolite dynamics rather well (Figure 5A). The main improvement of the best pairwise interaction model (Figure 5A) was a better fit to the short-term dynamics of 6-phosphogluconate. Thus, the most parsimonious explanation of all results is that the rapid drop of NADPH levels (Figure 2A) alleviates inhibition of G6P dehydrogenase to exploit the reserve capacity of the PP pathway, which, in turn, stabilizes NADPH levels within 15 s (Figure 5A, NAPDH).

The Reserve PP Pathway Flux Capacity Is Important for Oxidative Stress Resistance

Since the "reserve PP pathway flux capacity" during unstressed growth on glucose was readily released during the initial oxidative stress response, the results suggest that *E. coli* invests resources during normal growth to maintain the capacity for rapid stabilization of NADPH levels until transcriptional or other regulatory mechanisms can be implemented. Consequently, cells lacking such plasticity in the PP pathway should be more sensitive to oxidative stress. To test this hypothesis, we used a G6P isomerase deletion mutant (Δ*pgi*) with a block in upper glycolysis that therefore relies exclusively on the PP pathway for glucose catabolism (Figure 5B) (Canonaco et al., 2001; Usui et al., 2012). The resulting NADPH overproduction is balanced through the soluble transhydrogenase UdhA during steady-state growth of the mutant (Sauer et al., 2004). Since there is no known stress-specific signal to this transhydrogenase that is not normally active in the wild-type under our conditions, we hypothesized that this Δ*pgi* mutant has no means to rapidly increase its NADPH production with its PP pathway running already at

maximum capacity, hence should be more sensitive to oxidative stress. Although slowly growing strains are intrinsically more tolerant to stress (Gilbert et al., 1990; Claudi et al., 2014), the slow-growing Δ*pgi* mutant was indeed more sensitive to H_2O_2-mediated oxidative stress; i.e., the minimal inhibitory concentration was 10 mM compared with 20 mM for the wild-type (Figure 5C). Oxidative stress sensitivity of Δ*pgi* mutants has been reported before, but no convincing metabolic explanation was offered (Valdivia-González et al., 2012; Byrne et al., 2014).

Since the Δ*pgi* mutant has a different metabolism from wild-type, indirect influences on the cells' sensitivity to stress cannot be excluded. To more directly validate the reserve flux capacity, we hypothesized that oxidative stress sensitivity should scale with the reserve PP pathway flux capacity. Using a titratable G6P dehydrogenase (Zwf) *E. coli* strain, we gradually decreased the enzyme's expression level and hence the pathway's reserve capacity. Upon exposure to 20 mM H_2O_2, decreasing G6P dehydrogenase expression gradually increased the strain's sensitivity to the oxidative stress (Figures 5D and 6). Overall, our physiological results strongly support the conclusion of a reserve PP pathway flux capacity during normal growth that can be exploited upon stress to rapidly replenish increased cellular NADPH demand.

DISCUSSION

By combining dynamic metabolomics, ^{13}C labeling experiments, and computational modeling, we provided strong evidence for the key metabolic mechanisms that coordinate the immediate resistance to oxidative stress in *E. coli*. During unstressed steady-state growth, cells invest into a higher flux capacity of the oxidative PP pathway than required to support growth. Within seconds, this reserve capacity can be utilized primarily through the release of NADPH inhibition of G6P dehydrogenase to instantaneously increase the PP pathway flux for the reduction of NADPH from $NADP^+$. This valve-like mechanism enables a passive rapid response to any type of condition that depletes NADPH levels, such as the glutathione-dependent defense against ROS (Fang et al., 2002; Kohen and Nyska, 2002; Finkel, 2003; Stanton, 2012). We demonstrated that cells lacking such plasticity are much less tolerant to oxidative stress, presumably because they cannot rapidly and adequately reroute their flux toward the NADPH regenerating PP pathway.

Our findings highlight the importance of small molecule regulation in metabolism and the difficulty in understanding their overall function in a dynamic network context. The previously described oxidative damage of GAP dehydrogenase by ROS in yeast and mammalian cells (Ralser et al., 2007; Rui et al., 2010; Anastasiou et al., 2011) was necessary but not sufficient for *E. coli*. Computational and *in vitro* biochemical evidence identified the previously reported but not *in vivo* characterized NADPH inhibition of G6P dehydrogenase (Sanwal, 1970; Olavarría et al., 2012) as a second key regulation mechanism, and quantitatively explained its function in the immediate oxidative stress response.

To enable systematic mapping of allosteric interactions and to identify their functional relevance by ensemble modeling, we developed a more efficient computational framework that enables millions of simulations at a reasonable time frame. This partially scalable framework is based on principles from parallel computing, allowing us to exhaustively explore most possible structural combinations for our system. Beyond allosteric regulation of enzymes by small molecules, this approach and framework are applicable to any type of kinetic modeling where dynamic data have to be interpreted mechanistically to understand the system's regulatory circuit, for example in understanding kinase or transcription factor regulation (Arai et al., 2008; Soares et al., 2013; Schmidt et al., 2015; Drazic et al., 2016; Kochanowski et al., 2017).

STAR★METHODS

Detailed methods are provided in the online version of this paper and include the following:

- KEY RESOURCES TABLE
- EXPERIMENTAL MODEL AND SUBJECT DETAILS
  - Strains, Media and Perturbation
  - Cultivation and Experiments for the Determination of H_2O_2 MIC Concentrations in WT and Δ*pgi* *E. coli* Strains
  - Quantification of Intracellular Metabolite Concentrations
- METHOD DETAILS
  - Purification of Glucose-6-phosphate Dehydrogenase
  - *In Vitro* Enzymatic Assay to Determine Kinetic Parameters
  - Kinetic Model of Glycolysis/Gluconeogenesis and the Pentose Phosphate Pathway
  - Parallel Ensemble Modeling Framework
- QUANTIFICATION AND STATISTICAL ANALYSIS
  - Parameterization of the Kinetic Model of Glycolysis/-Gluconeogenesis and the Pentose Phosphate Pathway
  - Selection of the Best Parameter Set for Each Model Topology
  - Akaike Information Criterion (AIC)
  - Pairwise Average Rank
  - Biological Replicates and Analysis of Data
- DATA AND SOFTWARE AVAILABILITY

SUPPLEMENTAL INFORMATION

Supplemental Information includes four figures and six tables can be found with this article online at https://doi.org/10.1016/j.cels.2018.04.009.

ACKNOWLEDGMENTS

We thank Elad Noor, Andreas Kuehne, Mattia Zampieri, Michael Berney, and Nicola Zamboni for fruitful discussions and helpful suggestions. This work was funded by the Swiss Initiative in Systems Biology (SystemsX.ch) IPhD fellowship to D.C.

AUTHOR CONTRIBUTIONS

D.C., H.L., and U.S. conceived and designed the study. D.C. and H.L. performed the dynamic experiments. D.C. designed and implemented the parallel ensemble modeling framework, performed the computational analyses, and wrote the manuscript. T.F. performed the *in vitro* experiments and analysis of G6P dehydrogenase activity. K.K. assisted with experiments and L.G.

with computational analyses. D.C. and U.S. wrote the manuscript. All authors read and approved the final manuscript.

DECLARATION OF INTERESTS

The authors declare no competing financial interests.

Received: August 1, 2017
Revised: January 19, 2018
Accepted: April 10, 2018
Published: May 9, 2018

REFERENCES

Anastasiou, D., Poulogiannis, G., Asara, J.M., Boxer, M.B., Jiang, J., Shen, M., Bellinger, G., Sasaki, A.T., Locasale, J.W., Auld, D.S., et al. (2011). Inhibition of pyruvate kinase M2 by reactive oxygen species contributes to cellular antioxidant responses. Science *334*, 1278–1283.

Arai, H., Roh, J.H., and Kaplan, S. (2008). Transcriptome dynamics during the transition from anaerobic photosynthesis to aerobic respiration in *Rhodobacter sphaeroides* 2.4.1. J. Bacteriol. *190*, 286–299.

Baba, T., Ara, T., Hasegawa, M., Takai, Y., Okumura, Y., Baba, M., Datsenko, K.A., Tomita, M., Wanner, B.L., and Mori, H. (2006). Construction of *Escherichia coli* K-12 in-frame, single-gene knockout mutants: the Keio collection. Mol. Syst. Biol. *2*, 2006.0008.

Babtie, A.C., Kirk, P., and Stumpf, M.P.H. (2014). Topological sensitivity analysis for systems biology. Proc. Natl. Acad. Sci. USA *111*, 18507–18512.

Baez, A., and Shiloach, J. (2013). *Escherichia coli* avoids high dissolved oxygen stress by activation of SoxRS and manganese-superoxide dismutase. Microb. Cell Fact. *12*, 23.

Blanchard, J.L., Wholey, W.-Y., Conlon, E.M., and Pomposiello, P.J. (2007). Rapid changes in gene expression dynamics in response to superoxide reveal SoxRS-dependent and independent transcriptional networks. PLoS One *2*, e1186.

Brumaghim, J.L., Li, Y., Henle, E., and Linn, S. (2003). Effects of hydrogen peroxide upon nicotinamide nucleotide metabolism in *Escherichia coli*: changes in enzyme levels and nicotinamide nucleotide pools and studies of the oxidation of NAD(P)H by Fe(III). J. Biol. Chem. *278*, 42495–42504.

Byrne, R.T., Chen, S.H., Wood, E.A., Cabot, E.L., and Cox, M.M. (2014). *Escherichia coli* genes and pathways involved in surviving extreme exposure to ionizing radiation. J. Bacteriol. *196*, 3534–3545.

Canonaco, F., Hess, T.A., Heri, S., Wang, T., Szyperski, T., and Sauer, U. (2001). Metabolic flux response to phosphoglucose isomerase knock-out in *Escherichia coli* and impact of overexpression of the soluble transhydrogenase UdhA. FEMS Microbiol. Lett. *204*, 247–252.

Chassagnole, C., Noisommit-Rizzi, N., Schmid, J.W., Mauch, K., and Reuss, M. (2002). Dynamic modeling of the central carbon metabolism of *Escherichia coli*. Biotechnol. Bioeng. *79*, 53–73.

Chechik, G., Oh, E., Rando, O., Weissman, J., Regev, A., and Koller, D. (2008). Activity motifs reveal principles of timing in transcriptional control of the yeast metabolic network. Nat. Biotechnol. *26*, 1251–1259.

Claudi, B., Spröte, P., Chirkova, A., Personnic, N., Zankl, J., Schürmann, N., Schmidt, A., Bumann, D., Yan, D., Hwa, T., et al. (2014). Phenotypic variation of *Salmonella* in host tissues delays eradication by antimicrobial chemotherapy. Cell *158*, 722–733.

Drazic, A., Myklebust, L.M., Ree, R., and Arnesen, T. (2016). The world of protein acetylation. Biochim. Biophys. Acta *1864*, 1372–1401.

Fang, Y.-Z., Yang, S., and Wu, G. (2002). Free radicals, antioxidants, and nutrition. Nutrition *18*, 872–879.

Finkel, T. (2003). Oxidant signals and oxidative stress. Curr. Opin. Cell Biol. *15*, 247–254.

Fong, S.S., Marciniak, J.Y., and Palsson, B.Ø. (2003). Description and interpretation of adaptive evolution of *Escherichia coli* K-12 MG1655 by using a genome-scale in silico metabolic model. J. Bacteriol. *185*, 6400–6408.

Fuhrer, T., Fischer, E., and Sauer, U. (2005). Experimental identification and quantification of glucose metabolism in seven bacterial species. J. Bacteriol. *187*, 1581–1590.

Fuhrer, T., and Sauer, U. (2009). Different biochemical mechanisms ensure network-wide balancing of reducing equivalents in microbial metabolism. J. Bacteriol. *191*, 2112–2121.

Gerosa, L., Haverkorn van Rijsewijk, B.R.B., Christodoulou, D., Kochanowski, K., Schmidt, T.S.B., Noor, E., and Sauer, U. (2015). Pseudo-transition analysis identifies the key regulators of dynamic metabolic adaptations from steady-state data. Cell Syst. *1*, 270–282.

Gilbert, P., Collier, P.J., and Brown, M.R. (1990). Influence of growth rate on susceptibility to antimicrobial agents: biofilms, cell cycle, dormancy, and stringent response. Antimicrob. Agents Chemother. *34*, 1865–1868.

Grant, C.M. (2008). Metabolic reconfiguration is a regulated response to oxidative stress. J. Biol. *7*, 1.

Greenberg, J.T., and Demple, B. (1989). A global response induced in *Escherichia coli* by redox-cycling agents overlaps with that induced by peroxide stress. J. Bacteriol. *171*, 3933–3939.

Imlay, J.A. (2013). The molecular mechanisms and physiological consequences of oxidative stress: lessons from a model bacterium. Nat. Rev. Microbiol. *11*, 443–454.

Jia, G., Stephanopoulos, G., and Gunawan, R. (2012). Ensemble kinetic modeling of metabolic networks from dynamic metabolic profiles. Metabolites *2*, 891–912.

Kitagawa, M., Ara, T., Arifuzzaman, M., Ioka-Nakamichi, T., Inamoto, E., Toyonaga, H., and Mori, H. (2006). Complete set of ORF clones of *Escherichia coli* ASKA library (a complete set of *E. coli* K-12 ORF archive): unique resources for biological research. DNA Res. *12*, 291–299.

Kochanowski, K., Gerosa, L., Brunner, S.F., Christodoulou, D., Nikolaev, Y.V., and Sauer, U. (2017). Few regulatory metabolites coordinate expression of central metabolic genes in *Escherichia coli*. Mol. Syst. Biol. *13*, 903.

Kohen, R., and Nyska, A. (2002). Oxidation of biological systems: oxidative stress phenomena, antioxidants, redox reactions, and methods for their quantification. Toxicol. Pathol. *30*, 620–650.

Krüger, A., Grüning, N.-M., Wamelink, M.M.C., Kerick, M., Kirpy, A., Parkhomchuk, D., Bluemlein, K., Schweiger, M.-R., Soldatov, A., Lehrach, H., et al. (2011). The pentose phosphate pathway is a metabolic redox sensor and regulates transcription during the antioxidant response. Antioxid. Redox Signal. *15*, 311–324.

Kuehne, A., Emmert, H., Soehle, J., Winnefeld, M., Fischer, F., Wenck, H., Gallinat, S., Terstegen, L., Lucius, R., Hildebrand, J., et al. (2015). Acute activation of oxidative pentose phosphate pathway as first-line response to oxidative stress in human skin cells. Mol. Cell *59*, 359–371.

Link, H., Buescher, J.M., and Sauer, U. (2012). Targeted and quantitative metabolomics in bacteria. Methods Microbiol. *39*, 127–150.

Link, H., Christodoulou, D., and Sauer, U. (2014). Advancing metabolic models with kinetic information. Curr. Opin. Biotechnol. *29*, 8–14.

Link, H., Kochanowski, K., and Sauer, U. (2013). Systematic identification of allosteric protein-metabolite interactions that control enzyme activity in vivo. Nat. Biotechnol. *31*, 357–361.

Mishra, S., and Imlay, J. (2012). Why do bacteria use so many enzymes to scavenge hydrogen peroxide? Arch. Biochem. Biophys. *525*, 145–160.

Murakami, K., Tsubouchi, R., Fukayama, M., Ogawa, T., and Yoshino, M. (2006). Oxidative inactivation of reduced NADP-generating enzymes in *E. coli*: iron-dependent inactivation with affinity cleavage of NADP-isocitrate dehydrogenase. Arch. Microbiol. *186*, 385–392.

Nikolaev, Y.V., Kochanowski, K., Link, H., Sauer, U., and Allain, F.H.-T. (2016). Systematic identification of protein–metabolite interactions in complex metabolite mixtures by ligand-detected nuclear magnetic resonance spectroscopy. Biochemistry *55*, 2590–2600.

Nunoshiba, T., Hidalgo, E., Amábile Cuevas, C.F., and Demple, B. (1992). Two-stage control of an oxidative stress regulon: the *Escherichia coli* SoxR protein triggers redox-inducible expression of the soxS regulatory gene. J. Bacteriol. *174*, 6054–6060.

Olavarría, K., Valdés, D., and Cabrera, R. (2012). The cofactor preference of glucose-6-phosphate dehydrogenase from *Escherichia coli*—modeling the physiological production of reduced cofactors. FEBS J. *279*, 2296–2309.

Park, J.O., Rubin, S.A., Xu, Y.-F., Amador-Noguez, D., Fan, J., Shlomi, T., and Rabinowitz, J.D. (2016). Metabolite concentrations, fluxes and free energies imply efficient enzyme usage. Nat. Chem. Biol. *12*, 482–489.

Ralser, M., Wamelink, M.M., Kowald, A., Gerisch, B., Heeren, G., Struys, E.A., Klipp, E., Jakobs, C., Breitenbach, M., Lehrach, H., et al. (2007). Dynamic rerouting of the carbohydrate flux is key to counteracting oxidative stress. J. Biol. *6*, 10.

Ralser, M., Wamelink, M.M.C., Latkolik, S., Jansen, E.E.W., Lehrach, H., and Jakobs, C. (2009). Metabolic reconfiguration precedes transcriptional regulation in the antioxidant response. Nat. Biotechnol. *27*, 604–605.

Reznik, E., Christodoulou, D., Goldford, J.E., Briars, E., Sauer, U., Segrè, D., and Noor, E. (2017). Genome-scale architecture of small molecule regulatory networks and the fundamental trade-off between regulation and enzymatic activity. Cell Rep. *20*, 2666–2677.

Rui, B., Shen, T., Zhou, H., Liu, J., Chen, J., Pan, X., Liu, H., Wu, J., Zheng, H., and Shi, Y. (2010). A systematic investigation of *Escherichia coli* central carbon metabolism in response to superoxide stress. BMC Syst. Biol. *4*, 122.

Sandoval, J.M., Arenas, F.A., Vásquez, C.C., Purwantini, E., and Daniels, L. (2011). Glucose-6-phosphate dehydrogenase protects *Escherichia coli* from tellurite-mediated oxidative stress. PLoS One *6*, e25573.

Sanwal, B.D. (1970). Regulatory mechanisms involving nicotinamide adenine nucleotides as allosteric effectors. 3. Control of glucose 6-phosphate dehydrogenase. J. Biol. Chem. *245*, 1626–1631.

Sauer, U., Canonaco, F., Heri, S., Perrenoud, A., and Fischer, E. (2004). The soluble and membrane-bound transhydrogenases UdhA and PntAB have divergent functions in NADPH metabolism of *Escherichia coli*. J. Biol. Chem. *279*, 6613–6619.

Schmidt, A., Kochanowski, K., Vedelaar, S., Ahrné, E., Volkmer, B., Callipo, L., Knoops, K., Bauer, M., Aebersold, R., and Heinemann, M. (2015). The quantitative and condition-dependent *Escherichia coli* proteome. Nat. Biotechnol. *34*, 104–110.

Segal, I. (1975). Enzyme kinetics: behavior and analysis of steady-state and rapid equilibrium enzyme systems, Available at: https://scholar.google.com/scholar?q=Segal+enzyme+kinetics+behavior+and+analysis&btnG=&hl=en&as_sdt=0%2C5, (Accessed: 13 July 2017)

Seo, S.W., Kim, D., Szubin, R., and Palsson, B.O. (2015). Genome-wide reconstruction of OxyR and SoxRS transcriptional regulatory networks under oxidative stress in *Escherichia coli* K-12 MG1655. Cell Rep. *12*, 1289–1299.

Shimizu, K. (2013). Regulation systems of bacteria such as *Escherichia coli* in response to nutrient limitation and environmental stresses. Metabolites *4*, 1–35.

Soares, N.C., Spät, P., Krug, K., and Macek, B. (2013). Global dynamics of the *Escherichia coli* proteome and phosphoproteome during growth in minimal medium. J. Proteome Res. *12*, 2611–2621.

Stanton, R.C. (2012). Glucose-6-phosphate dehydrogenase, NADPH, and cell survival. IUBMB Life *64*, 362–369.

Sunnaker, M., Zamora-Sillero, E., Dechant, R., Ludwig, C., Busetto, A.G., Wagner, A., and Stelling, J. (2013). Automatic generation of predictive dynamic models reveals nuclear phosphorylation as the key Msn2 control mechanism. Sci. Signal. *6*, ra41.

Sunnaker, M., Zamora-Sillero, E., Lopez Garcia de Lomana, A., Rudroff, F., Sauer, U., Stelling, J., and Wagner, A. (2014). Topological augmentation to infer hidden processes in biological systems. Bioinformatics *30*, 221–227.

Turkheimer, F.E., Hinz, R., and Cunningham, V.J. (2003). On the undecidability among kinetic models: from model selection to model averaging. J. Cereb. Blood Flow Metab. *23*, 490–498.

Usui, Y., Hirasawa, T., Furusawa, C., Shirai, T., Yamamoto, N., Mori, H., and Shimizu, H. (2012). Investigating the effects of perturbations to pgi and eno gene expression on central carbon metabolism in *Escherichia coli* using 13 C metabolic flux analysis. Microb. Cell Fact. *11*, 87.

Valdivia-González, M., Pérez-Donoso, J.M., and Vásquez, C.C. (2012). Effect of tellurite-mediated oxidative stress on the *Escherichia coli* glycolytic pathway. Biometals *25*, 451–458.

Yuan, J., Bennett, B.D., and Rabinowitz, J.D. (2008). Kinetic flux profiling for quantitation of cellular metabolic fluxes. Nat. Protoc. *3*, 1328–1340.

Zheng, M., and Storz, G. (2000). Redox sensing by prokaryotic transcription factors. Biochem. Pharmacol. *59*, 1–6.

STAR★METHODS

KEY RESOURCES TABLE

REAGENT or RESOURCE	SOURCE	IDENTIFIER
Bacterial and Virus Strains		
E. coli BW 25113	KEIO collection (Baba et al., 2006)	N/A
Δ*pgi E. coli*	KEIO collection (Baba et al., 2006)	N/A
zwf titration strain	This paper	N/A
Chemicals, Peptides, and Recombinant Proteins		
H2O2 (Hydrogen Peroxide Solution)	Sigma-Aldrich	CAS # 7722-84-1
Software and Algorithms		
Parallel Ensemble Modelling Pipeline	This Paper	N/A

EXPERIMENTAL MODEL AND SUBJECT DETAILS

Strains, Media and Perturbation

E. coli BW 25113 was cultivated in 500-mL shake flasks with M9 minimal medium containing 2 g L^{-1} glucose. Shake flask cultures were grown exponentially to an optical density at 600 nm between 0.4 and 0.6, and 2 ml culture aliquots were vacuum-filtered on a 0.45 μm pore size nitrocellulose filter (Millipore) and perfused for 10 s with M9 medium containing 2 g L^{-1} glucose at 37°C. Oxidative stress perturbations were realized by changing the perfusion solution to M9 medium containing 2 g L^{-1} glucose plus 1 mM H_2O_2 (see also Figure S4 and (Link et al., 2013)). For labeling experiments the perfusion M9 medium contained 2 g L^{-1} [1-^{13}C] glucose with or without 1 mM H_2O_2 (control and stress condition respectively).

The *zwf* titration strain was constructed as follows. First, the *zwf* gene was cloned into the IPTG-titratable expression plasmid pTrc99KK (Link et al., 2013) (primer 1:GCCTCGAGATGGCGGTAACGCAAACAGCC,primer2:CGGGATCCTTACTCAAACTCATTC CAGGAACG), yielding plasmid pTrc99KK-*zwf*. This plasmid was then transformed into a *zwf* deletion strain obtained from the Keio collection (Baba et al., 2006). To exclude adverse effects on oxidative stress resistance merely due to protein overexpression, the *zwf* deletion strain was also transformed with a N-terminal his-tagged GFP titration plasmid, pTrc99KK-GFP:N-term HT, which was obtained from Nikolaev et al. (2016).

Cultivation and Experiments for the Determination of H_2O_2 MIC Concentrations in WT and Δ*pgi E. coli* Strains

All experiments were performed using M9 minimal medium (with 2 g L^{-1} glucose as the carbon source, from now on referred as minimal medium). Minimal medium batch cultures of wild type *E. coli* or Δ*pgi* from the KEIO collection (Baba et al., 2006) in 96-deep-well format plates (Kuehner AG, Birsfelden, Switzerland) were inoculated 1:50 from LB precultures and incubated overnight at 37°C under shaking. Subsequently, 96-well flat transparent plates (Nunc, Roskilde, Denmark) containing M9 medium (fill volume 200 ml) were inoculated with overnight cultures. Online measurements of optical density at 600 nm (OD600) and fluorescence (excitation wavelength: 500 nm, emission wavelength: 530 nm) were performed at 37°C with shaking using a plate reader (TECAN infinite M200, Tecan Group Ltd, Männedorf, Switzerland). During early exponential growth (OD600 around 0.3) the plate was taken out of the plate reader and different wells of the plate were treated with different levels of minimal medium with H_2O_2 of stress: control (0 mM H_2O_2), 0.5 mM, 1 mM, 2.5 mM, 5 mM, 10 mM, 15 mM, 20 mM, 25 mM, 30 mM, 35 mM and 40 mM of H_2O_2. MIC was calculated as the H_2O_2 concentration, where the post-stress growth rate of a culture is below 0.02 h^{-1}. All results stem from at least 4 individual biological replicates, for every different stress level.

Quantification of Intracellular Metabolite Concentrations

Shake flask cultures were grown exponentially to an optical density at 600 nm between 0.4 and 0.6, and 2 ml culture aliquots were vacuum-filtered on a 0.45 μm pore size nitrocellulose filter (Millipore) and perfused for 10 s with M9 medium containing 2 g L^{-1} glucose at 37°C. Oxidative stress perturbations were realized by changing the perfusion solution to M9 medium containing 2 g L^{-1} glucose plus 1 mM H_2O_2 (see also Figure S4 and (Link et al., 2013)). Metabolomics samples were taken after the annotated exposure to the stress perfusion solution (Figure S4) and were immediately quenched in 4 ml quenching/extraction solution (40% methanol, 40% acetonitrile, 20% H_2O, all v/v) at -20°C (Link et al., 2012). To normalize for variations in sample processing, 100 μl of a fully 13C-labeled E. coli internal metabolome extract was added. Samples were incubated for 2 h at −20°C, subsequently dried completely at 120 μbar (Christ RVC 2-33 CD centrifuge and Christ Alpha 2-4 CD freeze dryer), and stored at −80°C until measurements. Before measurements, samples were resuspended in 100 μl water, centrifuged for 5 min (5,000 g, 4°C) to remove residual particles, and transferred to V-bottomed 96-well sample plates (Thermo Fisher Scientific). Measurement, data acquisition, and data analysis were performed as described previously (Link et al., 2012). Briefly, separation of compounds was achieved by ion-pairing

ultrahigh performance liquid chromatography (UPLC) using a Waters Acquity UPLC with a Waters Acquity T3 end-capped reverse phase column (dimensions, 150 mm × 2.1 mm × 1.8 μm; Waters Corporation) and coupled to compound detection using a tandem mass spectrometer (Thermo TSQ Quantum Ultra triple quadrupole; Thermo Fisher Scientific). Data acquisition and peak integration was performed with in-house software. To determine the absolute concentration of metabolites, a 1:3 dilution series of a standard solution (containing more than 80 metabolites of central carbon metabolism) with ^{13}C internal standard was prepared and measured in parallel (see also Table S6).

METHOD DETAILS

Purification of Glucose-6-phosphate Dehydrogenase

Glucose-6-phosphate dehydrogenase was overexpressed in 50 ml LB medium with 0.1 mM IPTG and 25 mg/L chloramphenicol at 37°C and 250 rpm from an overexpression plasmid obtained from the ASKA clone collection (Kitagawa et al., 2006). Cells were harvested by centrifugation and the pellet was washed twice with 2 ml 0.9% NaCl with 10 mM $MgSO_4$. The pellet was then resuspended in 4 ml ice cold 100 mM Tris-HCl pH 7.5, 5 mM $MgCl_2$ supplemented with Protease-Inhibitor (Complete EDTA-free, Roche) and 1 mM DTT. Cells were disrupted by passage through a precooled French press mini cell at 1000 PSI and the crude extract was subsequently centrifuged for 30 min at 23000 x g and 4°C to obtain a clear cell lysate. The lysate was then loaded on a 1 ml HisTrap HP columns from Amersham Biosciences. The column was washed with 12 volumes of wash buffer (20 mM NaH_2PO_4 pH 7.5, 500 mM NaCl, 10 mM Imidazole, 15 mM β-Mercaptoethanol) and then the protein was eluted using increasing imidazole concentrations. Fractions containing pure protein were buffer-exchanged against 100 mM Tris-HCl pH 7.5, 10 mM MgCl2 and 15 mM β-Mercaptoethanol using 25 kD Spectra-Por Float-A-Lyzer (see also Figure S3).

In Vitro Enzymatic Assay to Determine Kinetic Parameters

All enzyme assays were run at 30°C in 100 mM Tris HCl pH7.5 and 10 mM $MgCl_2$ on a Spectramax Plus spectrometer (Molecular Devices). Absorbance was recorded at 340 nm with 2 second interval single measurements in 1 ml cuvettes. Purified enzyme was equilibrate with cofactor until absorbance at 340 nm was stable. The measured absorbance curve over time was regressed with a second order polynomial to determine the initial velocity at the time point when the second substrate was added and the sample was mixed. K_M values for glucose 6-phosphate dehydrogenase were determined from measurements were glucose-6-phosphate concentrations were varied from 50 μM to 400 μM, while the NADP+ concentrations were held constant between 20 μM and 150 μM. According to the proposed sequential ordered bi-bi-mechanism (Segal, 1975), it was expected that NADPH will inhibit competitively in respect to $NADP^+$ (Chassagnole et al., 2002). To determine the respective inhibition constant, reaction velocities were determined under different NADPH concentrations (150, 75 and 0 μM), the glucose-6-phosphate concentration was held at 400 μM and $NADP^+$ was varied from 10 to 60 μM. The K_M values for $NADP^+$ and glucose-6P and the K_D value for NADPH were then obtained by varying respective substrate or inhibitor concentrations and analysis by primary and secondary Lineweaver-Burk plots assuming a sequential two-substrate mechanism (Chassagnole et al., 2002):

$$V_{G6PDH} = \frac{V_{max}[NADP^+][G6P]}{k_{D,NADP^+}k_{M,G6P} + k_{M,G6P}[NADP^+] + k_{M,NADP^+}[G6P] + [NADP^+][G6P]} \quad \text{(Equation 1)}$$

Inhibition by NADPH was determined to be competitive with respect to $NADP^+$ which can be included by the following inhibitory terms (Chassagnole et al., 2002):

$$V_{G6PDH} = \frac{V_{max}[NADP^+][G6P]}{k_{D,NADP^+}k_{M,G6P}\left(1 + \frac{[NADPH]}{k_{i,NADPH}}\right) + k_{M,G6P}[NADP^+] + k_{M,NADP^+}[G6P]\left(1 + \frac{[NADPH]}{k_{i,NADPH}}\right) + [NADP^+][G6P]} \quad \text{(Equation 2)}$$

Kinetic Model of Glycolysis/Gluconeogenesis and the Pentose Phosphate Pathway

The model (and its stoichiometry) considered are shown in Figure 2A in the main text.

The irreversible reactions and transport of glucose are described by Michaelis-Menten kinetics:

$$v = v_{max}\frac{c_{Substrate}}{c_{Substrate} + K_M}$$

Similar to previous studies (Link et al., 2013) we assume that reversible reactions are near equilibrium and the law of mass action describes the kinetics for the forward (+) and backward (−) direction in these cases.

$$v^+ = k^+ c_{Substrate}$$

$$v^- = k^- c_{Product}$$

The detailed equations are given below:

Kinetic Rate Equations – Irreversible Reactions

Reaction 1

glucose specific phosphotransferase system

$$v_{PTS} = v_{max,PTS}\frac{c_{Glucose}}{c_{Glucose} + K_{PTS,Glucose}}$$

Reaction 2

phosphofructokinase (PFK)

$$v_{PFK} = v_{max,PFK}\frac{c_{F6P}}{c_{F6P} + K_{PFK,F6P}}$$

Reaction 3

fructose-1,6-bisphosphatase (FBPase)

$$v_{\mathrm{FBPase}} = v_{max,\mathrm{FBPase}}\frac{c_{FBP}}{c_{FBP} + K_{\mathrm{FBPase},FBP}}$$

Reaction 4

glucose-6-phosphatedehydrogenase (G6PDH)

$$v_{\mathrm{G6PDH}} = v_{max,\mathrm{G6PDH}}\frac{c_{G6P}}{c_{G6P} + K_{\mathrm{G6PDH},G6P}}$$

Reaction 5

6-phosphogluconate dehydrogenase (GND)

$$v_{\mathrm{GND}} = v_{max,\mathrm{GND}}\frac{c_{6PG}}{c_{6PG} + K_{\mathrm{GND},6PG}}$$

Reaction 6

pyruvate kinase (PYK)

$$v_{\mathrm{PYK}} = v_{max,\mathrm{PYK}}\frac{c_{PEP}}{c_{PEP} + K_{\mathrm{PYK},PEP}}$$

Reaction 7

phosphoenolpyruvate synthetase (PPS)

$$v_{\mathrm{PPS}} = v_{max,\mathrm{PPS}}\frac{c_{PYR}}{c_{PYR} + K_{\mathrm{PPS},PYR}}$$

Reaction 8

pyruvate dehydrogenase (PDH)

$$v_{\mathrm{PDH}} = v_{max,\mathrm{PDH}}\frac{c_{PYR}}{c_{PYR} + K_{\mathrm{PDH},PYR}}$$

Reaction 9

phosphoenolpyruvate carboxylase (PPC)

$$v_{\mathrm{PPC}} = v_{max,\mathrm{PPC}}\frac{c_{PEP}}{c_{PEP} + K_{\mathrm{PPC},PEP}}$$

Kinetic Rate Equations – Reversible Reactions

Reaction 10/11

phosphoglucoseisomerase (PGI)

$$v^{+}_{\mathrm{PGI}} = k^{+}_{PGI}c_{G6P}$$

$$v^{-}_{\mathrm{PGI}} = k^{-}_{PGI}c_{F6P}$$

Reaction 12/13

fructose-1,6-bisphosphate aldolase (ALD).

Instead of GAP and DHAP this reaction produces 2 molecules DHAP, since we assume that GAP and DHAP are in equilibrium by triose phosphate isomerase.

$$v^{+}_{\mathrm{ALD}} = k^{+}_{\mathrm{ALD}}c_{FBP}$$

$$v^{-}_{ALD} = k^{-}_{ALD} c_{DHAP} c_{DHAP}$$

Reaction 14/15

glyceraldehyde-3-phosphate dehydrogenase (GAPDH), phosphoglucokinase (PGK), phosphoglucomutase (PGM) and enolase (ENO) are in equilibrium (Link et al., 2013) and lumped into one reaction.

$$v^{+}_{GAPDH} = k^{+}_{GAPDH} c_{DHAP}$$

$$v^{-}_{GAPDH} = k^{-}_{GAPDH} c_{PEP}$$

Reaction 16/17

transketolase A (TKTA)

$$v^{+}_{TKTA} = k^{+}_{TKTA} c_{P5P}$$

$$v^{-}_{TKTA} = k^{-}_{TKTA} c_{DHAP} c_{S7P}$$

Reaction 18/19

transketolase B (TKTB)

$$v^{+}_{TKTB} = k^{+}_{TKTB} c_{P5P} c_{E4P}$$

$$v^{-}_{TKTB} = k^{-}_{TKTB} c_{DHAP} c_{F6P}$$

Reaction 20/21

transaldolase (TALA)

$$v^{+}_{TALA} = k^{+}_{TALA} c_{DHAP} c_{S7P}$$

$$v^{-}_{TALA} = k^{-}_{TALA} c_{E4P} c_{F6P}$$

Reaction 22

biosynthetic E4P drain (E4PD)

$$v^{+}_{E4PD} = k^{+}_{E4PD} c_{E4P}$$

Reaction 23

biosynthetic P5P drain (P5PD)

$$v^{+}_{P5PD} = k^{+}_{P5PD} c_{P5P}$$

Reaction 24

anabolic proxy of NADPH drain (NADPHD)

$$v^{+}_{NADPHD} = k^{+}_{NADPHD} c_{NADPH}$$

Reaction 25

generation of ROS from external source (ROSG)

this reaction is implemented as a constant input (that we vary in the different simulations)

$$v^{+}_{ROSG} = k^{+}_{ROSG}$$

Reaction 26

scavenging of ROS with NADPH (ROSS)

$$v^{+}_{ROSS} = k^{+}_{ROSS} c_{ROS}$$

Kinetic Rate Equations: Small Molecule – Enzyme Interactions

An interaction between an enzyme catalyzing reaction *i* and a small molecule *j* is included as a power law term affecting the reaction rate.

$$v^{*}_{i} = v_{max,i} \prod_{j} \left(c_j / c_{j,0} \right)^{a_{i,j}}$$

In the base model without interactions (except the one from ROS on GAPDH), all exponents $a_{i,j}$ are zero and therefore the power law terms equal to 1. With this model we managed to easily search the topological space by testing ensembles of structurally different models by setting the according exponent to real-valued numbers. With this approach we also managed to create a parallel algorithm that does so efficiently.

Ordinary Differential Equations (ODEs)

$$\frac{\mathrm{dG6P}}{\mathrm{dt}} = \mathrm{Reaction1} - \mathrm{Reaction4} - \mathrm{Reaction10} + \mathrm{Reaction11} =$$

$$= v_{max,PTS}\frac{c_{Glucose}}{c_{Glucose} + K_{PTS,Glucose}} - v_{max,\mathrm{G6PDH}}\frac{c_{G6P}}{c_{G6P} + K_{\mathrm{G6PDH},G6P}} - k^{+}_{PGI}c_{G6P} + k^{-}_{PGI}c_{F6P}$$

$$\frac{\mathrm{dF6P}}{\mathrm{dt}} = -\mathrm{Reaction2} + \mathrm{Reaction3} + \mathrm{Reaction10} - \mathrm{Reaction11} + \mathrm{Reaction18} - \mathrm{Reaction19} + \mathrm{Reaction20} - \mathrm{Reaction21}$$

$$\frac{\mathrm{dFBP}}{\mathrm{dt}} = \mathrm{Reaction2} - \mathrm{Reaction3} - \mathrm{Reaction12} + \mathrm{Reaction13}$$

$$\frac{\mathrm{dDHAP}}{\mathrm{dt}} = 2 \times \mathrm{Reaction12} - 2 \times \mathrm{Reaction13} - \mathrm{Reaction14} + \mathrm{Reaction15} + \mathrm{Reaction16} - \mathrm{Reaction17} + \mathrm{Reaction18} - \mathrm{Reaction19} - \mathrm{Reaction20} + \mathrm{Reaction21}$$

$$\frac{\mathrm{d6PG}}{\mathrm{dt}} = \mathrm{Reaction4} - \mathrm{Reaction5}$$

$$\frac{\mathrm{dPEP}}{\mathrm{dt}} = -\mathrm{Reaction1} - \mathrm{Reaction6} + \mathrm{Reaction7} - \mathrm{Reaction9} + \mathrm{Reaction14} - \mathrm{Reaction15}$$

$$\frac{\mathrm{dPYR}}{\mathrm{dt}} = \mathrm{Reaction1} + \mathrm{Reaction6} - \mathrm{Reaction7} - \mathrm{Reaction8}$$

$$\frac{\mathrm{dP5P}}{\mathrm{dt}} = \mathrm{Reaction5} - 2 \times \mathrm{Reaction16} + 2 \times \mathrm{Reaction17} - \mathrm{Reaction18} + \mathrm{Reaction19} - \mathrm{Reaction23}$$

$$\frac{\mathrm{dE4P}}{\mathrm{dt}} = -\mathrm{Reaction18} + \mathrm{Reaction19} + \mathrm{Reaction20} - \mathrm{Reaction21} - \mathrm{Reaction22}$$

$$\frac{\mathrm{dS7P}}{\mathrm{dt}} = \mathrm{Reaction16} - \mathrm{Reaction17} - \mathrm{Reaction20} + \mathrm{Reaction21}$$

$$\frac{\mathrm{dNADPH}}{\mathrm{dt}} = \mathrm{Reaction4} + \mathrm{Reaction5} - \mathrm{Reaction24} - \mathrm{Reaction26}$$

$$\frac{\mathrm{dROS}}{\mathrm{dt}} = \mathrm{Reaction25} - \mathrm{Reaction26}$$

Parallel Ensemble Modeling Framework

Initially a model containing the biochemical reactions displayed in Figure 3A plus an inhibition directly from ROS to GAPDH is created. This base model serves as the scaffold/template for every other model topology, which is implemented by augmenting the base model with one or two metabolite-enzyme interactions. All the different (~12000) model topologies are populated as different model objects in one *master* server and then are consequently sent to different CPU cores - *workers* for simulation, using the High Performance Computing service of ETH (Figure 3C), containing over 29000 processor cores with a theoretical performance reaching over 1000 teraflops. Depending on how many CPU cores are available, the time of computation for all the simulations (which depend on the number of model topologies and the number of different parameter sets we test for every model, in our case 12000 topologies and 2000 parameter sets yield ~24 million simulations) scales accordingly. Once the simulations from the different CPU cores – *workers* are finished, the saved simulated results return to the *master*, where they are processed and analyzed thus yielding the rank of every interaction, based on the criteria we have set (frequency and score). All code was written in MATLAB and various functions from the Parallel Computing toolbox and the SimBiology toolbox were used.

QUANTIFICATION AND STATISTICAL ANALYSIS

Parameterization of the Kinetic Model of Glycolysis/Gluconeogenesis and the Pentose Phosphate Pathway

Kinetic parameters followed from statistical sampling of unknown parameters and a steady analysis as described below.

K_M Values

The K_M values were randomly sampled from an interval of 0.1-10 times the *in vitro* determined literature value.

Steady State Analysis and Statistical Sampling

In order to determine V_{max} values we performed a steady state analysis using measured glucose uptake rate (1.17 mM/s). Metabolic fluxes were estimated by flux balance analysis during growth on glucose (Fong et al., 2003) and we considered uncertainties about the fluxes by taking into account measured flux distributions (Gerosa et al., 2015) and by statistical sampling of 5 parameters:

1. Futile cycling between PFK and FBPase: $v_{FBPase,0} - v_{PFK,0}/v_{FBPase,0} = 0 - 1$
2. Futile cycling between PYK and PPS: $v_{PPS,0} - v_{PYK,0}/v_{PPS,0} = 0 - 1$
3. PP pathway flux: 15-40% of the glucose uptake
4. Biosynthetic drain of pentoses (P5P) and E4P: 50-70% of the PP pathway flux
5. Immediate increase in ROS flux: 0.5 – 1

The steady state reaction rates (v^0) of all reactions follow from these unknown flux ratios and the measured glucose rate. Subsequently, the V_{max} of reaction *i* follows from v_i^0, the sampled $K_{i,M}$ and the measured steady state concentrations c_j^0 of the particular small molecule:

$$v_{i,max} = v_i^0 \left(1 + K_{i,M} \Big/ c_j^0\right)$$

Rate Constants of Reversible Reactions

In the case of reversible reactions, we statistically sample for every pair (e.g. reactions 10/11) the efficiency of this reaction: if we know that a glycolytic flux of 1 goes through this reaction pair in the glycolytic direction and the efficiency is 0.5, this means that reaction 10 will have a flux of 2 and reaction 11 a flux of 1. The rate constants k^+ and k^- are calculated following this approach.

Selection of the Best Parameter Set for Each Model Topology

As described in the main text, we randomly sampled P = 20000 for each of the models with single small-molecule enzyme interactions and P = 2000 for each of each model with pairs of small-molecule enzyme interactions. For each parameter set, the simulation was performed with MATLAB. The residuals between the simulated species (indicated by $'$) and the measured species are calculated at t=5 time points for s = 8 species where we have absolute concentrations for. Due to differences in the absolute metabolite concentrations we estimated the sum of squared errors for s=8 relative metabolite concentrations ($\tilde{c}$) that are normalized to the glucose steady state concentrations:

$$SSR_c = \sum_{s=1}^{8} \sum_{t=1}^{5} \left(\widetilde{c'_{s,t}} - \widetilde{c_{s,t}} \right)^2$$

We used this objective to select the best parameter set for each model topology.

Akaike Information Criterion (AIC)

In order to compare in a systematic manner the simulation results of models with different topologies and different number of parameters *K* (due to different numbers of small-molecule – enzyme interactions), we utilized the Akaike Information Criterion (AIC) (Link et al., 2013; Turkheimer et al., 2003).

$$AIC = N\log(SSR/N) + 2K$$

where N is the total number of residuals. A particular model X with small molecule – enzyme interactions is ranked relative to the base model by the difference of AICs:

$$\Delta AIC_{ModelX} = AIC_{BaseModel} - AIC_{ModelX}$$

Pairwise Average Rank

The ranks of the pairwise interactions based on how often the interaction appears in models with ΔAIC>0 (frequency) and the best ΔAIC that was achieved with a model including this interaction, were taken into account in the calculation of the average rank of the interactions. The average rank of an interaction i is calculated as the mean of the two individual ranks that a certain interaction has achieved.

Biological Replicates and Analysis of Data

In every case, the average values and the standard deviation result from three independent experiments, unless otherwise stated. The analysis of the (experimental and simulated) data was performed using custom MATLAB (MathWorks) software. MATLAB was used for all simulations and the kinetic model was partly implemented using the SimBiology toolbox. The model is detailed in Supplemental Information. The p-values displayed in Figure 6, were calculated using the ttest function, MATLAB (MathWorks). Significance was evaluated based on the calculated p-value (significance for p-value < 0.05).

DATA AND SOFTWARE AVAILABILITY

The data generated in this work are available as Tables S1 and S6.

Cell Systems, Volume *6*

Supplemental Information

Reserve Flux Capacity in the Pentose Phosphate Pathway Enables *Escherichia coli*'s Rapid Response to Oxidative Stress

Dimitris Christodoulou, Hannes Link, Tobias Fuhrer, Karl Kochanowski, Luca Gerosa, and Uwe Sauer

Supplemental Information

Reserve flux capacity in the pentose phosphate pathway enables *Escherichia coli*'s rapid response to oxidative stress

Dimitris Christodoulou, Hannes Link, Tobias Fuhrer, Karl Kochanowski, Luca Gerosa, Uwe Sauer

Supplementary Figures

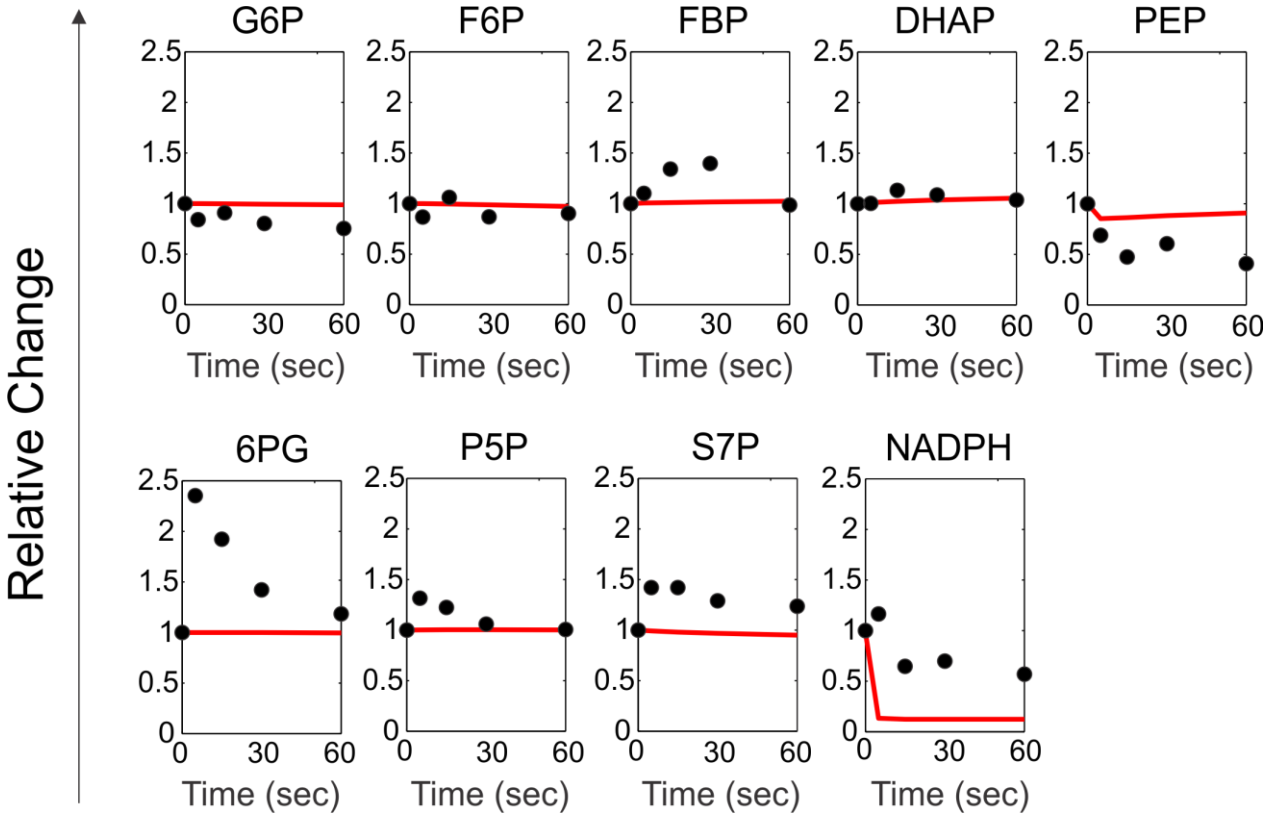

Figure S1. Related to Figure 5: Base model (model amended with the ROS inhibition of GAPDH) simulation results (red solid line) against the experimental data (black dots). Y axis represents the relative change of a particular metabolite, compared to the untreated condition (time point 0).

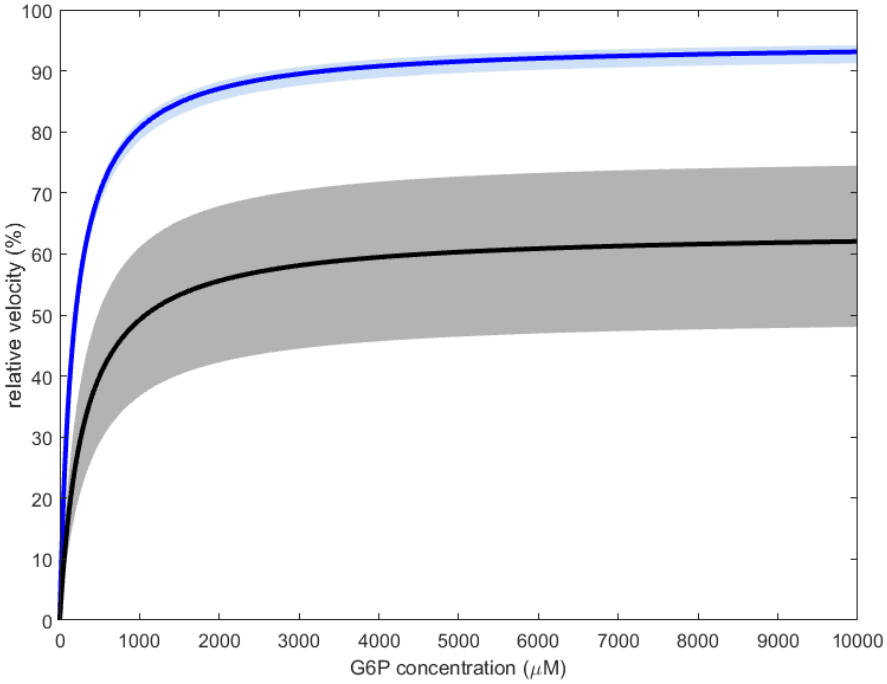

Figure S2. Related to STAR Methods: Simulated reaction velocities for glucose-6-phosphate dehydrogenase using rate laws without NADPH inhibition (blue line, Supplementary Methods Equation 1) and with NADPH inhibition (black line, Supplementary Methods Equation 2). Experimentally determined kinetic parameters were used (mean values from Table S1) and the pool of NADPH and $NADP^+$ was assumed to be approximately 500µM, well above measured dissociation, inhibition constants and K_M. The shaded areas are created by testing different NADP/NADPH ratios. Only the forward reaction with NADPH inhibition was simulated since the 6P-gluconolactone produced reacts rapidly further to 6P-gluconate and in addition is very instable[1]. G6P concentration during growth on glucose in wild type *E. coli* is in the range of 1-2 mM, with mutant strain Δpgi having approximately 10 times higher concentrations[2].

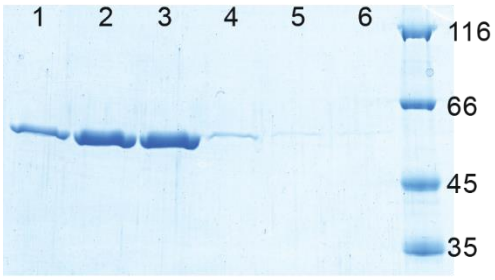

Figure S3. Related to STAR Methods: SDS-PAGE of overexpressed and His-Tag purified glucose-6P dehydrogenase (~56.8 kD including His-Tag). The pure enzyme was eluted with different imidazole concentrations (lanes 1 to 6: 100-200, 200, 200-300, 300, and twice 500 mM imidazole). Fractions in lane 2 and 3 were pooled and used for further analysis.

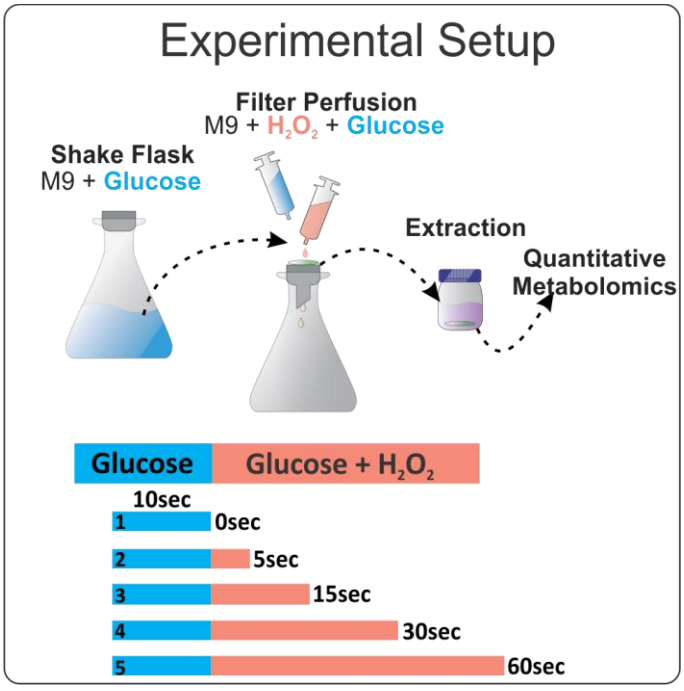

Figure S4. Related to STAR Methods: Experimental setup for fast carbon-source switching. Culture broth from a shake flask is transferred onto a nitrocellulose filter mounted on a vacuum device. Subsequently cells are continuously perfused with medium containing glucose and are then switched to a freshly prepared medium containing glucose and H_2O_2. Upon filtration the filter is extracted in cold acetonitrile/methanol/water mix and cell extracts are analyzed by ultrahigh performance liquid chromatography– tandem mass spectrometry. Lower panel, perfusion profiles of samples before extraction. Cyan bars, perfusion with glucose medium; orange bars, with glucose and H_2O_2 medium.

Supplementary Tables

Table S1. Related to Figure 5: Experimentally determined kinetic parameters of **G6P dehydrogenase** and intracellular metabolite concentrations

	This study [μM]	Olavarria et al* [μM]
Kinetic Parameters[a]:		
Substrate K_M:		
$NADP^+$	23	7.5 ± 0.8
glucose-6-phosphate	136	174 ± 11
$NADP^+$ dissociation K_i:		
$NADP^+$	90	19 ± 4
NADPH inhibition K_i:		
$K_{ic,NADP+}$	35	14 ± 2
$K_{ic,glucose-6-phosphate}$	100	101 ± 9
Relative reaction rates[b]		
2 mM Fructose- 1,6-bisphosphate (FBP)	98	-

[a] Own values were obtained from primary and secondary Lineweaver-Burk plots and were confirmed by non-linear regression fits with the corresponding rate laws.

[b] Normalized to reaction rate in absence of inhibitor, using 25 μM $NADP^+$ and 125 μM as substrate, standard deviations were below 5% from triplicate experiments.

* Olavarría, K., Valdés, D. & Cabrera, R. The cofactor preference of glucose-6-phosphate dehydrogenase from Escherichia coli--modeling the physiological production of reduced cofactors. *FEBS J.* **279,** 2296–309 (2012).

Table S2. Related to Figure 3: Kinetic parameters of reactions in the glycolysis – PP pathway model. V_{max} of irreversible reactions are estimable parameters and no value is given.

Reaction	Parameter	Value Range
Irreversible Reactions		
PFK	$V_{max,PFK}$	-
	$K_{PFK,F6P}$	$(0.1\text{-}10) \cdot 0.16\text{mM}$[1]
FBPase	$V_{max,FBPase}$	-
	$K_{FBPase,FBP}$	$(0.1\text{-}10) \cdot 0.015\text{mM}$[2]
G6PDH	$V_{max,\ G6PDH}$	-
	$K_{G6PDH,G6P}$	$(0.1\text{-}10) \cdot 0.2\text{mM}$[3]
GND	$V_{max,GND}$	-
	$K_{GND,6PG}$	$(0.1\text{-}10) \cdot 0.1\text{mM}$[4]
PYK	$V_{max,PYK}$	-
	$K_{PYK,PEP}$	$(0.1\text{-}10) \cdot 0.31\text{mM}$[5]
PPS	$V_{max,PPS}$	-
	$K_{PPS,PYR}$	$(0.1\text{-}10) \cdot 0.083\text{mM}$[6]
PDH	$V_{max,PDH}$	-
	$K_{PDH,PYR}$	$(0.1\text{-}10) \cdot 0.515\text{mM}$[7]
PPC	$V_{max,PPC}$	-
	$K_{PPC,PEP}$	$(0.1\text{-}10) \cdot 0.19\text{mM}$[8]

1. Zheng, R. L. & Kemp, R. G. The mechanism of ATP inhibition of wild type and mutant phosphofructo-1-kinase from Escherichia coli. *J. Biol. Chem.* **267,** 23640–5 (1992).
2. Kelley-Loughnane, N. *et al.* Purification, kinetic studies, and homology model of Escherichia coli fructose-1,6-bisphosphatase. *Biochim. Biophys. Acta - Protein Struct. Mol. Enzymol.* **1594,** 6–16 (2002).
3. Westwood, A. W. & Doelle, H. W. Glucose 6-phosphate and 6-phosphogluconate dehydrogenases and their control mechanisms in Escherichia coli K-12. *Microbios* **9,** 143–65 (1974).
4. de Silva, A. O. & Fraenkel, D. G. The 6-phosphogluconate dehydrogenase reaction in Escherichia coli. *J. Biol. Chem.* **254,** 10237–42 (1979).
5. Boiteux, A., Markus, M., Plesser, T., Hess, B. & Malcovati, M. Analysis of progress curves. Interaction of pyruvate kinase from Escherichia coli with fructose 1,6-bisphosphate and calcium ions. *Biochem. J.* **211,** 631–40 (1983).
6. Berman, K. M. & Cohn, M. Phosphoenolpyruvate synthetase of Escherichia coli. Purification, some properties, and the role of divalent metal ions. *J. Biol. Chem.* **245,** 5309–18 (1970).
7. Nemeria, N. *et al.* Inhibition of the Escherichia coli Pyruvate Dehydrogenase Complex E1 Subunit and Its Tyrosine 177 Variants by Thiamin 2-Thiazolone and Thiamin 2-Thiothiazolone Diphosphates: EVIDENCE FOR REVERSIBLE TIGHT-BINDING INHIBITION. *J. Biol. Chem.* **276,** 45969–45978 (2001).
8. Kai, Y. *et al.* Three-dimensional structure of phosphoenolpyruvate carboxylase: a proposed mechanism for allosteric inhibition. *Proc. Natl. Acad. Sci. U. S. A.* **96,** 823–8 (1999).

Table S3. Related to Table 1: Rank of the interactions, as inferred from our combined computational-experimental approach. Pairwise average rank (5^{th} column) was calculated as the average of the different ranks each interaction achieved in individual metrics, namely frequency and score, stemming from the results of approximately 24 million pairwise simulations. Enzymes affected by metabolites (activated or inhibited) are shown in columns 2, 3 and 4 of the table, respectively.

Table S4. Related to Table 1: Rank of all 162 interactions that were tested in models with pairwise allosteric interactions. Both frequency and score metrics are displayed. Ranking is based on how often the interaction appears in models with ΔAIC>0 (frequency).

Table S5. Related to Table 1: Rank of all 162 interactions displaying the AIC of models with single interactions relative to the base model. Ranking is based on the best ΔAIC that was achieved with a model including only this interaction.

Table S6. Related to Figure 1, Figure 2 and STAR Methods: Metabolite data of the H_2O_2 perturbation. The standard deviation (s.d.) results from three independent experiments. Time (in seconds) demonstrates the time of exposure to H_2O_2, after 10 seconds washing with glucose minimal medium (see STAR Methods)